Trees talk tremor - Wood anatomy and δ13C content reveal contrasting tree-growth responses to earthquakes

Christian H. Mohr[1], Michael Manga[2], Gerhard Helle[3], Ingo Heinrich[3], Laura Giese[4], and Oliver Korup[1]

[1]University of Potsdam
[2]University of California, Berkeley
[3]Helmholtz Centre Potsdam
[4]German Federal Institute of Hydrology

November 26, 2022

Abstract

Moderate to large earthquakes can increase the amount of water feeding stream flows, raise groundwater levels, and thus grant plant roots more access to water in water-limited environments. We examine tree growth and photosynthetic responses to the Maule M_w 8.8 Earthquake in small headwater catchments of Chile's Mediterranean Coastal Range. We combine high-resolution wood anatomic (lumen area) and biogeochemical (of wood cellulose) proxies of daily to weekly tree growth on cores sampled from trees on floodplains and close to ridge lines. We find that, immediately after the earthquake, at least two out of six tree cores show changes in these proxies: lumen area increased and decreased in the valley trees, whereas the sign of change was reversed in trees on the hillslope. Our results indicate a control of soil water on this response, largely consistent with models that predict how enhanced post-seismic vertical soil permeability causes groundwater levels to rise on the valley floor, but fall along the ridges. Statistical analysis with boosted regression trees indicates that streamflow discharge gained predictive importance for photosynthetic activity on the ridges but lost importance on the valley floor after the earthquake. We infer that earthquakes may stimulate ecohydrological conditions favoring tree growth over days to weeks by triggering stomatal opening. The weak and short-lived signals that we identified, however, show that such responses are only valid under water-limited instead of energy-limited tree growth. Hence, dendrochronological studies targeted at annual resolution may overlook some earthquake effects on tree vitality.

Trees talk tremor – Wood anatomy and δ^{13}C content reveal contrasting tree-growth responses to earthquakes

Christian H. Mohr[1], Michael Manga[2], Gerhard Helle[3], Ingo Heinrich[3], Laura Giese[4], Oliver Korup[1,5]

[1]Institute of Environmental Science and Geography, University of Potsdam, Germany

[2]Department of Earth and Planetary Science, University of California, 307 McCone Hall, Berkeley, CA 94720, USA

[3]GFZ German Research Centre for Geosciences, Telegrafenberg, 14473 Potsdam, Germany

[4]German Federal Institute of Hydrology (BfG), 56002 Koblenz, Germany

[5]Institute of Geosciences, University of Potsdam, Germany

Corresponding author: Christian Mohr (cmohr@uni-potsdam.de)

Key Points:

- Earthquakes may stimulate tree growth by promoting photosynthesis
- Direction of tree growth change depends on local topographic position
- First dendro-ecohydrological study to explore earthquake-water-vegetation interactions at scale of cells

Abstract

Moderate to large earthquakes can increase the amount of water feeding stream flows, raise groundwater levels, and thus grant plant roots more access to water in water-limited environments. We examine tree growth and photosynthetic responses to the Maule M_w 8.8 Earthquake in small headwater catchments of Chile's Mediterranean Coastal Range. We combine high-resolution wood anatomic (lumen area) and biogeochemical ($\delta^{13}C$ of wood cellulose) proxies of daily to weekly tree growth on cores sampled from trees on floodplains and close to ridge lines. We find that, immediately after the earthquake, at least two out of six tree cores show changes in these proxies: lumen area increased and $\delta^{13}C$ decreased in the valley trees, whereas the sign of change was reversed in trees on the hillslope. Our results indicate a control of soil water on this response, largely consistent with models that predict how enhanced post-seismic vertical soil permeability causes groundwater levels to rise on the valley floor, but fall along the ridges. Statistical analysis with boosted regression trees indicates that streamflow discharge gained predictive importance for photosynthetic activity on the ridges but lost importance on the valley floor after the earthquake. We infer that earthquakes may stimulate ecohydrological conditions favoring tree growth over days to weeks by triggering stomatal opening. The weak and short-lived signals that we identified, however, show that such responses are only valid under water-limited instead of energy-limited tree growth. Hence, dendrochronological studies targeted at annual resolution may overlook some earthquake effects on tree vitality.

Plain Language Summary

Earthquakes deform and shake the surface and the ground below. These changes may affect groundwater flows. Groundwater level may rise in the valley bottom and drop along higher elevated ridges. Trees depend on such groundwater resources, particularly in dry climates. Hence, we expect contrasting responses of trees after earthquakes: at higher elevations, access to groundwater may be impeded, but enabled more in the valley bottoms. Thus, earthquake-enhanced tree growth should be pronounced only on valley floors, with opposite responses happening along ridges. We test this hypothesis in Pine forest plantations that were affected by the 2010 Maule earthquake, Chile. We find that tree growth increased following the earthquake

because of enhanced photosynthesis on valley floors, but decreased on upper hillslopes due to increased water stress. Overall, these responses are small but measurable. Our study is the first to combine state-of-the-art isotopic and wood anatomic proxies that we quantified at the cellular scale. Our results provide novel insights into the impacts of earthquakes on soil water and tree growth at an unprecedented daily to weekly resolution.

1 Introduction

Large prehistoric earthquakes are preserved in the geological record. Traditional archives of paleoseismology, the discipline concerned with reconstructing such earthquakes, include offsets in fault scarps and river channels, sediment deformation and soil liquefaction, landslide and tsunami deposits [*Ludwig*, 2015], and archeological records [*Nur*, 2007]. Biological archives mostly rely on damage to vegetation. For example, the sudden subsidence of coasts during earthquakes may submerge and kill near-shore vegetation [*Atwater and Yamaguchi*, 1991]. Shaking-induced damage to roots and damage from debris may suppress tree growth and be recorded in annual growth rings [*Bekker*, 2004; *Jacoby et al.*, 1997; *Lin and Lin*, 1998; *Meisling and Sieh*, 1980; *Page*, 1970]. Tree growth can also be enhanced if neighboring and competing trees died due to earthquakes [*Veblen et al.*, 1992], with larger individuals having the greatest survival potential [*Allen et al.*, 2020]. Earthquakes may elevate groundwater levels by increasing soil permeability and thus allowing trees more access to water and higher root water uptake [*Bekker et al.*, 2018; *Mohr et al.*, 2015]. Earthquakes as small as magnitude 4.6 have measurably affected tree growth [*Sheppard and White*, 1995]. Trees offer some advantages over geological archives of past seismic shaking. Trees are abundant and may thus better constrain earthquake magnitude and location [*Jacoby*, 1997], and tree rings offer a yearly resolution that is more accurate than most geochronological tools [*Jacoby et al.*, 1988; *Sheppard and Jacoby*, 1989].

Here we assess whether and how tree rings record a hydrological response to earthquakes. The principal mechanisms invoked to explain hydrological changes following large earthquakes include pore-pressure response to seismic static or elastic strain [*Muir-Wood and King*, 1993; *Wakita*, 1975], permeability changes caused by seismic waves [*Elkhoury et al.*, 2006; *Rojstaczer and Wolf*, 1992; *Wang et al.*, 2004], fluid migration along seismogenic dilatant cracks or crustal ruptures [*Sibson and Rowland*, 2003; *Tsunogai and Wakita*, 1996] or consolidation potentially up to liquefaction of sediments [*Manga*, 2001; *Manga et al.*, 2003;

Montgomery and Manga, 2003]. Seismic shaking may also mobilize water from the unsaturated zone [*Breen et al.*, 2020; *Mohr et al.*, 2015]. If tree growth is limited mainly by water [*Babst et al.*, 2019], trees should in theory record hydrological responses to earthquakes by changing their growth rates.

Two commonly observed hydrological responses to earthquakes are falling groundwater levels along ridges and increased stream discharge owing to permeability increases [*Rojstaczer et al.*, 1995; *Wang et al.*, 2004]. These responses can persist for weeks to months and modify regional water balances [*Mohr et al.*, 2017]. Many mechanisms for these changes have been proposed and debated [*Manga and Wang*, 2015]. One dramatic biological manifestation of these hydrological changes was the contrasting response of trees to the M 8 New Madrid, USA, earthquakes in 1811. *Lyell* [1849] reported that "all the trees of a date prior to 1811, although standing erect and entire, are dead and leafless.... [on the] higher level plain, where the dead trees stand . . . At the lower level are seen cypresses and cotton-wood, and other trees which delight in wet ground, all newer than 1812." (p.1235). The growth surge in surviving bald cypress (Taxodium distichum) in the two years after the 1811 earthquakes was the largest ever recorded for this species in the southeastern United States [*Arsdale et al.*, 1998].

From this observation, we hypothesize that strong ground shaking promotes tree growth close to streams, but impedes tree growth on hillslopes. We consider the response of trees in Chilean mountain catchments impacted by the M_w 8.8 Maule earthquake on February 27, 2010. First, we test whether rates of tree growth responded to the earthquake. Second, we assess whether this response outweighs other influences on growth such as rainstorms [*Carvalho et al.*, 2015]. We discuss whether it is possible to objectively identify seismic signals in tree rings even without knowing the exact timing of the earthquake. *Álvarez et al.*, [2012] and *Ojeda et al.* [2018] reported highly variable, rainfall-driven, growth in pine plantations within or close to the rupture zone of the Maule earthquake. Similarly, we expect possible earthquake signals in trees on weekly to monthly, but not necessarily annual, time scales. Most studies that searched for earthquake signals in trees analyzed the width of annual growth rings [*Fu et al.*, 2020]. Here, we focus instead on changes in wood anatomy at the cell-scale and on carbon isotopes as these may provide a connection between the growth of trees and the ecohydrological changes induced by the earthquake [*Galle et al.*, 2010]. We test whether changes in tree growth can be a novel proxy

for identifying past earthquakes at an unprecedented temporal resolution afforded by studying individual wood cells.

Stable carbon isotope analysis has become an important tool to trace eco-hydro-physiological processes in dendroecology [*Gessler et al.*, 2014]. $\delta^{13}\mathrm{C}$ measures the ratio of stable carbon isotopes ^{13}C to ^{12}C [*McCarroll and Loader*, 2004]. Following *Reynolds-Henne et al.* [2007], the isotopic ratios in tree rings most strongly reflect conditions of the current growing season. The fractionation of ^{13}C in wood occurs during photosynthetic diffusion and assimilation by the RuBisCo enzyme [*Farquhar and Sharkey*, 1982] because ^{13}C is heavier than ^{12}C and thus diffuses slower [*O'Leary*, 1988], forming slightly stronger chemical bonds. This isotopic discrimination is recorded in the living wood [e.g., *Dupouey et al.*, 1993; *Helle and Schleser*, 2004a, b; *Warren et al.*, 2001]. For low temperatures, high water supply or a combination of both, stomata apertures expand and RuBisCO preferentially assimilates ^{12}C from an abundant atmospheric pool, thus lowering $\delta^{13}\mathrm{C}$. In contrast, water stress, high temperatures or a combination of both, cause stomata apertures to decrease and reduce water loss through transpiration. Hence photosynthetic diffusion is restricted and assimilation by RuBisCO may be less “picky” in terms of preferring ^{12}C, thus $\delta^{13}\mathrm{C}$ increases [*Helle and Schleser*, 2004b].

At the beginning of the vegetation period, tree growth depends on reserves that are mainly stored as starch from the previous year(s). Following a three-phase-model established for broad-leaf trees, a lag-effect of starch storage may arise at the beginning of the vegetation period provoking $\delta^{13}\mathrm{C}$ enrichment [*Helle and Schleser*, 2004a]. This model predicts (1) enrichment in $\delta^{13}\mathrm{C}$ of early wood that is followed by (2) a decline during latewood formation and (3) another increase at the end of each vegetation period, that is, the last part of the latewood domain. The increase in $\delta^{13}\mathrm{C}$ in latewood happens at the end of the growing season due to same carbohydrate metabolism processes that enrich $\delta^{13}\mathrm{C}$ during early wood formation. $\delta^{13}\mathrm{C}$ is also sensitive to atmospheric CO_2 concentration as $\delta^{13}\mathrm{C}$ discrimination in plants is related to the ratio of the CO_2 concentrations within the stomatal cavity and the ambient atmosphere [e.g., *Farquhar et al.*, 1980; *Keeling et al.*, 2017].

Wood anatomy is also sensitive to (seasonal) changes in soil water [*Ziaco et al., 2016*]. *Carvalho et al.* [2015] found a high correlation between lumen area (LA) and soil moisture in water-limited Mediterranean conifer forests. Lumen is the membrane-defined intercellular space

inside the elongated cells in the xylem of vascular plants called tracheids; lumen area is the cross-sectional surface area [*Ziaco et al.*, 2016]. Assuming a sufficiently high number of tracheids formed per growing season and hydrological effects of earthquakes that persist for weeks to months [*Manga and Wang*, 2015], effects on tree growth should be recorded in wood anatomy. Seasonal patterns in $\delta^{13}\mathrm{C_{OM}}$ and lumen area reflect the interaction between seasonal micro-meteorological factors, soil water, and plant response to its evaporative environment [e.g., *Gessler et al.*, 2014]. Given potential access to shallow groundwater, earthquakes may cause favorable ecohydrological conditions and stimulate tree growth over days to weeks by triggering stomatal opening. We expect such boosting, however, under climatic conditions only that are favorable for tree growth, i.e. water stress relief by providing additional water to the plants. Thus, combining both wood anatomy and $\delta^{13}\mathrm{C}$ could be a proxy of tree growth and transpiration [*Galle et al.*, 2010]. To our knowledge, this is the first study of ecohydrological responses to earthquakes using stable isotopes and cell-level wood anatomy.

2 Study area, hydroclimatic conditions, and Maule earthquake

We study the response of *Pinus radiata* D. Don trees in two headwater catchments of the Chilean coast range (Fig. 1). The catchments, Pichún and San Antonio (SA), are equipped with streamflow water stage samplers, rain gauges, and air temperature loggers. These devices have been operated since 04/2008 [*Huber et al.*, 2010] and used for hydrological and geomorphic responses to the Maule earthquake [*Mohr et al.*, 2015; *Mohr et al.*, 2012] and forestry [*Barrientos et al.*, 2020; *Mohr et al.*, 2013; *Mohr et al.*, 2014].

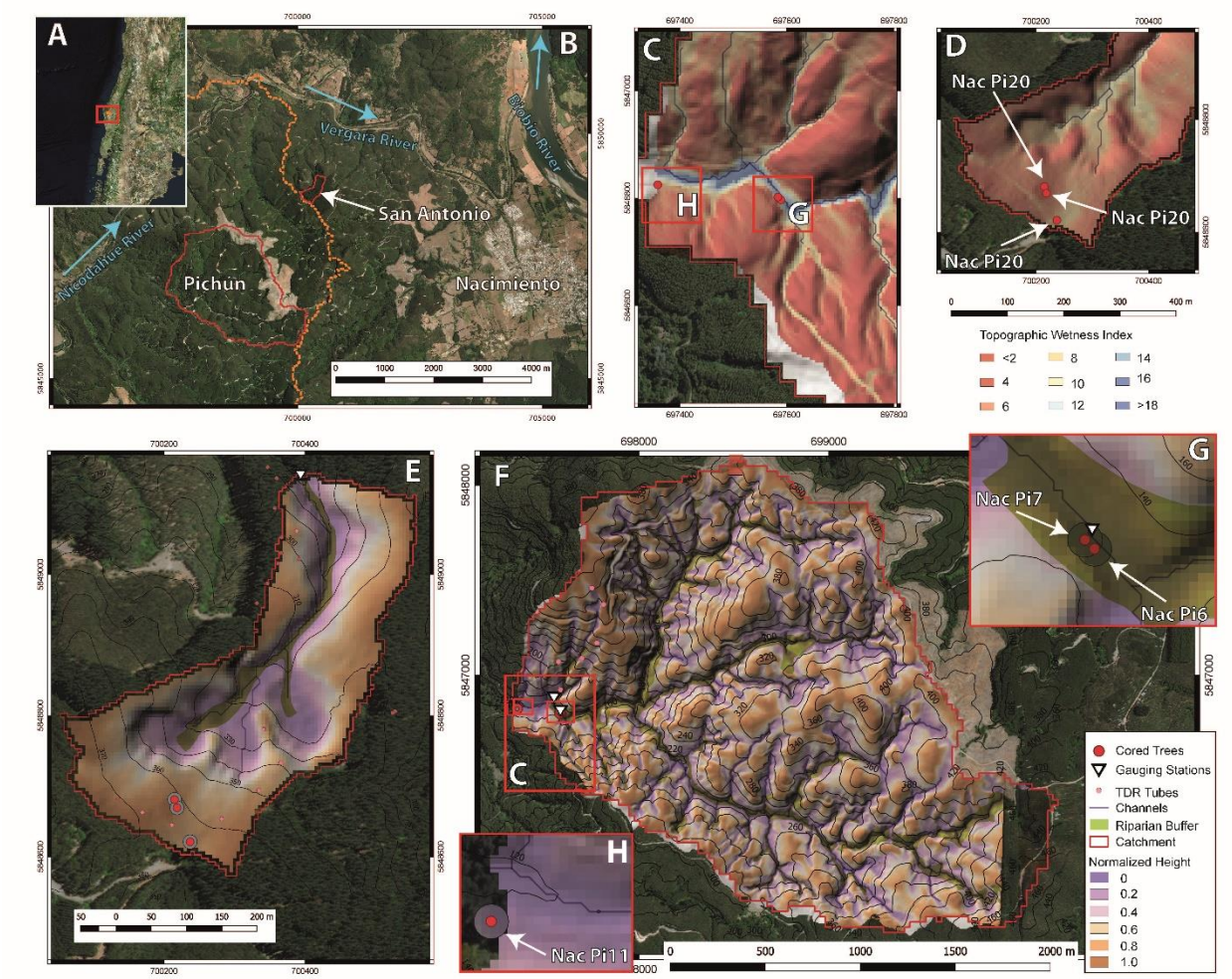

Figure 1. Study area. **a)** Overview of study area in south-central Chile and (**b**) San Antonio and Pichún catchments: The Nicodahue River catchment is outlined by orange dots. Estimated topographic wetness Indices (TWI), relative slope positions for Pichún (**c, f**) and San Antonio (**d, e**); Location of the cored trees are depicted by red circles; Pink circles are TDR-Trime Access tubes for soil water monitoring and white triangles are streamflow gauges. Contour intervals are 10 m and 20 m for San Antonio and Pichún, respectively. **g** and **h** show loactions of the cored trees.

Both catchments are geologically and topographically similar [*Mohr et al.*, 2012]. The dominant soil type is Luvisol. Schist bedrock is exposed in the channel beds and alluvial deposits are present only locally. SA covers 0.13 km^2 with elevations from 270 to 380 m asl and mostly southeast-facing hillslopes; Pichún has 4.39 km^2 with elevations between 320-480 m asl (Fig. 1) with mainly south-facing hillslopes. At the time of the 2010 earthquake, SA had mature (~25

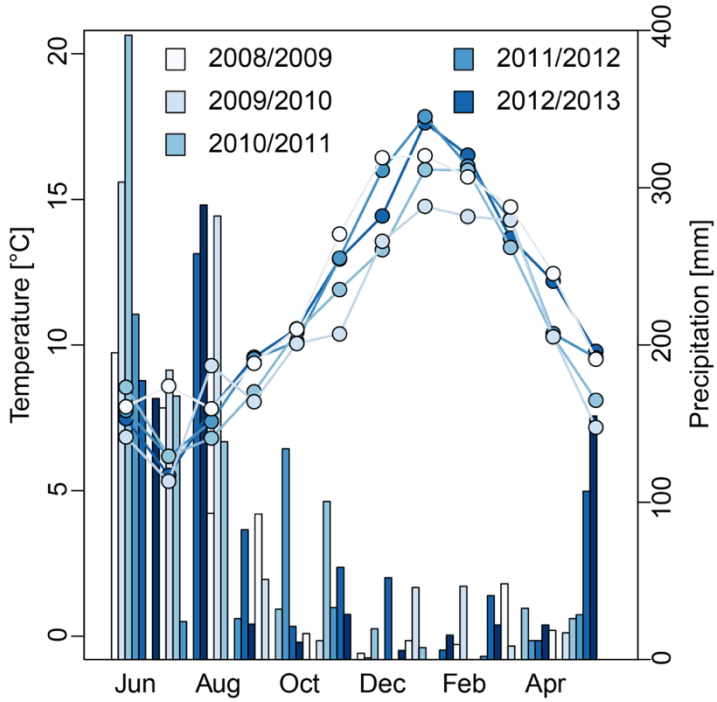

Figure 2. Monthly mean air temperature [°C] and precipitation [mm] during the growing seasons of 2008-2012; The catchment-averaged CR2MET data are from Nicodahue (#8362001, Fig. 1) in the CAMELS-CL data set [*Alvarez-Garreton et al.*, 2018].

	Temperature [°C]			Precipitation [mm]		
	T_{all}	T_{winter}	T_{summer}	P_{all}	P_{winter}	P_{summer}
1965-2013	11.2	7.4	12.5	951	510	440
$\bar{X}_{2008\text{-}13}$	11.2	7.3	12.5	890	611	374
$\sigma_{2008\text{-}13}$	0.55	0.47	0.78	205	159	40
2008/2009	11.7	8.1	13.2	890	619	424
2009/2010	10.4	7.1	11.4	1098	753	387
2010/2011	10.8	7.2	12.0	1056	674	393
2011/2012	11.5	7.1	13.0	733	669	330
2012/2013	11.5	6.9	13.0	620	340	337

Table 1. Temperature and rainfall for 2008 to 2012. T and P refer to mean temperatures [°C] and precipitation [mm]. The subscript $_{all}$ refers to an entire year, whereas $_{summer}$ and $_{winter}$ indicate mean temperature and precipitation during the dry summer months (Sep-May), and wet winter months (Oct-April), respectively; $\bar{X}$ (and σ) is the mean (standard deviation) for 2008-2013. Data are from Nicodahue (#8362001) in the CAMEL-CL dataset [*Alvarez-Garreton et al.*, 2018].

years old) *Pinus radiata* D.Don plantation forest, whereas Pichún had two-year old *Eucalyptus spp*. seedlings with shallow (<1 m) roots. Deeper-rooting (>2 m on average) native species such as Arrayán (*Luma apiculata* DC. Burret), Boldo (*Peumus boldus* Mol.), Roble (*Nothofagus obliqua* Mirb.) and exotic *Pinus radiata* D.Don were restricted to a 0.45 km^2 riparian buffer along the main stream [*Mohr et al.*, 2012]. *Pinus radiata* may produce >150 tracheids per growing season [*Skene*, 1969], thus providing a high temporal resolution.

According to *Peel et al.* [2007], the climate is Mediterranean (Csb) with a rainy season in the Austral winter and a hot, dry summer (Fig. 2). The mean air temperature and rainfall during the growing season is 11.2 °C and 951 mm, respectively (Table 1). The inter-annual hydroclimatic conditions between the studied growing periods had standard deviations $\sigma = 205$ mm and $\sigma = 0.55$ °C for mean annual precipitation and air temperature (Table 1). Among all growing seasons, those of 2011/12 and 2012/13 were extraordinarily dry and part of the multi-year Central Chile Mega Drought [*Garreaud et al.*, 2020].

Both catchments were in the rupture zone of the 2010 M_w 8.8 Maule earthquake that caused local peak ground velocities (PGV) of ~24 and 26 cm/s on the ridge and the valley bottom, respectively, for ~150 seconds [*Moreno et al.*, 2010; *Vigny et al.*, 2011]. The earthquake induced streamflow responses across south-central Chile yielded >1 km^3 of excess discharge [*Mohr et al.*, 2017]. Groundwater models estimated an increase in evapotranspiration of 30%–60% for at least 5-10 days after the earthquake before new rainfall commenced [*Mohr et al.*, 2015].

3 Data and Methods

We sampled six *Pinus radiata* D.Don. trees to study their wood anatomy and $\delta^{13}C$ composition. We extracted cores with a standard 40-cm Haglöfs increment corer of 4 mm inner diameter. We sampled all trees from four directions, i.e. upslope, downslope and parallel to the local slope direction, to account for reaction wood due to gravity [*Du and Yamamoto*, 2007]. Samples were collected on 16 and 17 February 2014. We took samples from the valley-floor and hillslope ridges (Fig. 1) to check whether our tree data from these different topographic locations might reveal different subsurface responses to the earthquake and thus changes in water

availability. We used several additional tree specific covariates that explicitly account for subsurface hydrology: (1) topographic wetness index (TWI), (2) aspect, (3) distance from the nearest stream, (4) relative hillslope height, and (5) the topographic position index (TPI) (Table 2, see Text S.1.1). We ran all spatial computations in QGIS 3.2.2 and SAGA 2.3.2. Fig. 3 and Text S.1.2. show the schematic workflow including all key lab analyses and data processing steps.

Table 2. Topographic measures for a 10-m buffer around the cored trees

	Sample ID					
Covariate	NacPi6	NacPi7	NacPi11	NacPi20	NacPi25	NacPi30
Altitude (m asl)	130.55 ±1.62	129.9 ±1.79	124.64 ±1.40	361.88 ± 0.32	361.84 ± 0.94	362.55 ±0.99
TWI	11.9±3.6	11.0±3.9	6.7±1.3	7.5±0.4	4.8±0.2	4.7±0.3
Aspect (°)	138.6±126.0	117.5±121.1	9.2±5.2	83.1±12.2	55.2±2.0	62.6±4.9
Distance from stream (m)*	4.01	4.04	30.6	108.5	93.9	94.3
Relative Height	0.01±0.01	0.02±0.01	0.19±0.07	0.78±0.01	0.90±0.02	0.88±0.04
TPI	-1.60±0.25	-1.61±0.28	-1.20+-0.15	0.11±0.03	0.66±0.04	0.59±0.07

We selected tree cores according to three criteria: (1) accurate dating and highly correlated measurements with an existing master reference curve; (2) distinct and straight tree ring borders; and (3) minimal number of features such as false, narrow or missing rings. Six out of 24 cores met these criteria and were used in our analyses. Four to six trees were sufficient to approximate a “hypothetical perfect chronology” for isotope studies [*Leavitt*, 2010]. We used data on streamflow, rainfall, temperature, and potential evapotranspiration [*Hargreaves and*

Samani, 1985] from our monitoring campaigns in the catchments [*Huber et al.*, 2010] (Fig. 1, 2) and from the CR2MET data for the Nicodahue catchment (#8362001) in the CAMEL-CL dataset [*Alvarez-Garreton et al.*, 2018]. The Nicodahue catchment is the receiving basin of both Pichún and San Antonio catchments. All statistical *p*-values mentioned in the text refer to the Wilcoxon rank-sum test.

3.1 Timing of cell differentiation within annual growing cycle, intra- and inter-annual dating

Field-measured diameters at breast height (DBH) (Courtesy, Oscar Maradones, Forestry SA Mininco, Table S1) indicate that the growing season begins in June. To account for and propagate the uncertainties regarding the timing of the growth measurements and the accuracy of DBH measurements, we ran n = 10,000 Monte Carlo simulations of seasonal DBH growth. We assumed a uniform uncertainty of ±10 days for the date of the DBH measurements and a uniform measurement accuracy of ±1%. We estimated a date for each tracheid cell and δ^{13}C-increment using the Gompertz growth model [*Rossi et al.*, 2003], which is widely used for dating xylem growth over growing seasons of conifers, including *Pinus radiata* [*Drew and Downes*, 2018]:

$$y = A\exp[-e^{(\beta - kt)}], \tag{1}$$

which we solved for the time of cell formation (t)

$$t = \frac{\beta - \ln[\ln(\frac{A+1}{y})]}{\mathrm{k}} \tag{2}$$

where y is cumulative number of cells, A is the asymptotic maximum number of cells, β is a location parameter, k is a rate change parameter (1/t), and t is time in days starting on June 1 ($t = t_1$). To avoid infinite values, we fixed the upper asymptote at A + 1 [*Rossi et al.*, 2003]. We normalized the cumulative tree growth so that during a given growing season we can establish a

sub-annual chronology regardless of both the number of tracheid cells (for wood anatomy) and the ~100 µm-increments used for sampling δ^{13}C.

We performed the inter-annual dating of the tree rings by measuring tree-ring width with WinDendro (Regent Instruments, Canada), and cross-dating all sampled cores with TsapWin (Rinntech, Heidelberg) and COFECHA [*Holmes*, 1983]. WinDendro is an image analysis tool to measure tree-ring width. Based on the scanned images, WinDendro semi-automatically measures the distances and angles between annual tree rings to estimate their width. This cross-dating is required in order to minimize errors within single tree cores owing to correlations among the samples.

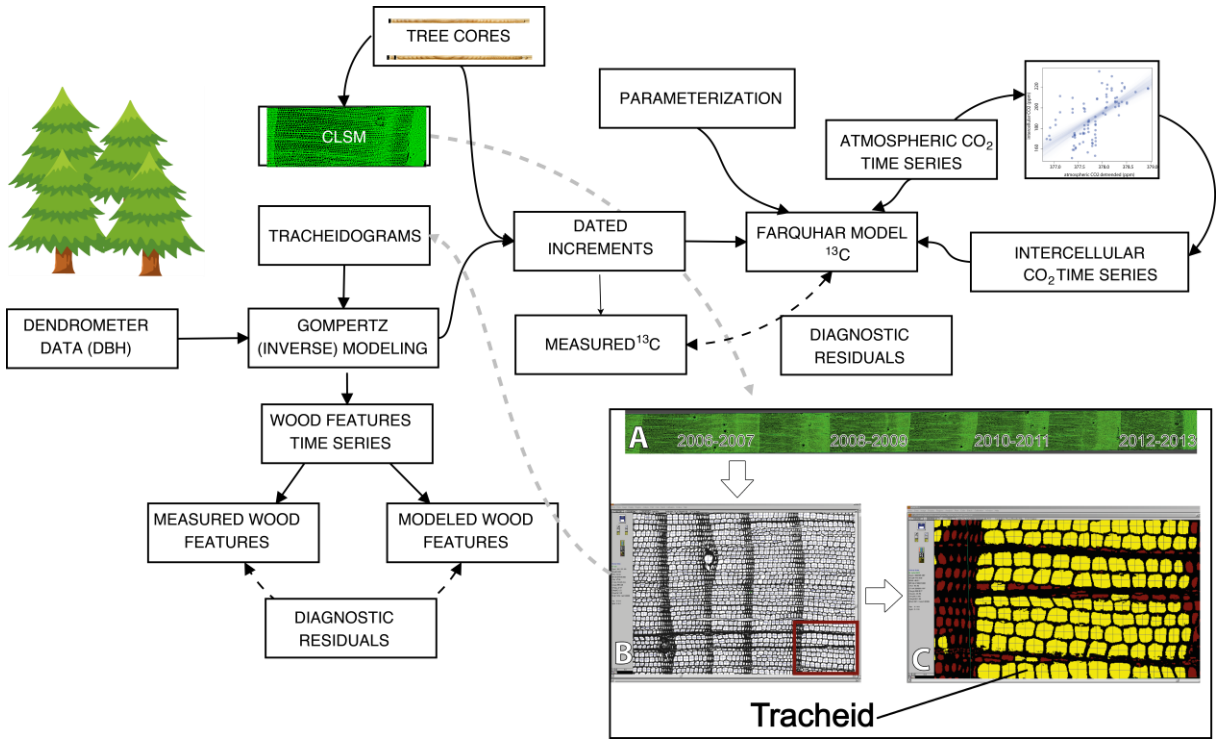

Figure 3. Overview of the workflow. **a, b** and **c** in the inset show a close-up of the working steps needed to obtain tracheidograms from the CLSM image (**a**); **b** and **c** show example screenshots of the WinCell application, with horizontal yellow bands illustrating single measurement paths.

3.2 Wood anatomy using confocal laser scanning

Our setup consists of a light microscope (Olympus BX51) and a Confocal Laser Scanning Microscope (CLSM, Olympus FV3-3F3). The CLSM system uses a helium-neon laser [Liang et al., 2013] with a wavelength of 543 nm as light source, a condenser, a color splitter, a microscope objective, a confocal aperture, an emission filter, and a detector (photomultiplier, PMT). The detection wavelength is 650 ± 50 nm; Pinhole: 3 (Airy); Objective: x10/ Numerical Aperture = 0.3. We refer to [*Liang et al.*, 2013] for technical details on the CLSM at the German Research Centre for Geosciences (GFZ), Potsdam, Germany.

3.2.1 Measurement of cell parameters

We measured lumen area (LA), lumen diameter (LD), cell-wall thickness (CWT), and cell diameter (CD) using WinCell (Regent Instruments, Canada), a software developed for wood anatomic image analysis. We focus on lumen area, which is particularly sensitive to changes in soil water [*Carvalho et al.*, 2015]. We manually drew the tree ring boundaries using WinCell and tagged each tree ring with the corresponding year. WinCell connects two adjacent tree rings and creates ‘measurement regions’ as the area between two subsequent rings. Within such regions, all tracheids were measured. Next, WinCell defines eight measurement paths by selecting eight cell rows that run in the radial direction from one tree ring boundary to the next [*Seo et al.*, 2014]. One tracheid measurement path thus chronologically reflects the variations in cell growth from the beginning to the end of one growing season (Fig. 3).

Tracheidograms show LA across the annual growth ring of a tree. Each cell line usually has an individual number of tracheids. To make tree rings comparable within a tree or from different trees, we normalized the number of cells per growing season along each path to the mean number of cells per hillslope position [*Rossi et al.*, 2003], i.e. ridge (n = 159) and valley bottom (n = 108). These values agree well with reported cell numbers for *Pinus radiata* [*Skene*, 1969]. We calculated tracheidograms with the R package tgram [*de la Cruz and De Soto*, 2017].

3.3 Inter-and intra-annual $\delta^{13}\mathrm{C}$ sampling of tree rings

To differentiate between atmospheric $\delta^{13}\mathrm{C}$ and $\delta^{13}\mathrm{C}$ contained in organic matter, we use subscripts $_{\mathrm{atm}}$ and $_{\mathrm{OM}}$. We performed all laboratory work at the dendrochronological laboratory at GFZ Potsdam, largely following the protocol by *Schollaen et al.* [2015, 2017].

High-resolution intra-annual sampling was performed by using an UV-Laser microdissection microscope (LMD7000, LEICA Microsystems,Wetzlar, Germany). The annual rings were subdivided into several subsections of approx. 100 µm in the radial direction using a pen screen. The number of sub-sections per ring was mostly >20 and varied depending on the tree-ring width (Supplementary Table 2). Every sub-section defined on the pen screen was dissected with the UV-laser beam and collected in a single tin capsule standing in a collection holder. The capsules were sealed and put onto an autosampler of a high temperature pyrolysis furnace Isoprime mass spectrometer (Elementar, Hanau, Germany) coupled online to a Carlo Erba NA 1500 elemental analyzer. The isotopic composition of the carbon compound was expressed as relative differences of the $^{13}C/^{12}C$ ratio of tree material with respect to the Vienna Pee-Dee Belemnite (VPDB) standard.

3.3.1 Modelling of intercellular CO_2 concentrations

We compared the measured $\delta^{13}\mathrm{C_{OM}}$ values against modeled $\delta^{13}\mathrm{C_{OM}}$ values. To this end, we first rearranged the photosynthesis model by *Farquhar et al.* [1980]

$$\delta^{13}\mathrm{C_{OM}} = \delta^{13}\mathrm{C_{atm}} + \epsilon_D * \frac{(1 - c_i)}{c_{atm}} + \epsilon_C * \frac{c_i}{c_{atm}} \tag{3}$$

to solve for leaf intercellular CO_2 concentrations (c_i) in the seasons 2008-2009 and 2011-2012 that we assumed to be unaffected by the earthquake or any starch storage at the beginning of the growing season [*Helle and Schleser*, 2004a]

$$c_i = \frac{c_{atm} * (\epsilon_D + \delta^{13}\mathrm{C_{atm}} - \delta^{13}\mathrm{C_{OM}})}{(\epsilon_D - \epsilon_C)} \tag{4}$$

where c_{atm} is the atmospheric CO_2 concentration (ppm), ϵ_D is the fractionation for diffusion (-4.4‰), $\delta^{13}\mathrm{C_{atm}}$ is atmospheric ^{13}C concentration (-8‰), and ϵ_C is fractionation at the CO_2 fixing enzyme, RuBisCo (-30‰). $\delta^{13}\mathrm{C_{OM}}$ is the measured isotope fractionation of the cellulose samples; values for ϵ_D and $\delta^{13}\mathrm{C_{atm}}$ are from *Helle and Schleser* [2004b]. Atmospheric CO_2 samples were collected at weekly to monthly intervals in a 5-liter evacuated glass flask and returned to Scripps Institution of Oceanography, where CO_2 concentrations (ppm) were determined [*Keeling and Whorf*, 2004]. Given that both the concentration and seasonal fluctuations in c_{atm} are weaker in the southern than the northern hemisphere [*Keeling et al.*, 2001], we used values from Baring Head, New Zealand [*Keeling et al.*, 2001] to stand in for missing local or regional data.

To correct for the anthropogenic increase in atmospheric CO_2, we detrended c_{atm} by decomposing the c_{atm} time series into seasonal trend and irregular components using R's loess function with default parameterization [*R Core Team*, 2020]. We regressed the undisturbed c_i using a linear model of the detrended ambient atmospheric CO_2 concentration c_{atm} (Fig. S2):

$$c_i = a + b\, c_{atm}, \tag{5}$$

where *a* is the model intercept and *b* is the model slope. The fitted c_i feeds back into (3) yielding

$$\delta^{13}C_{OM\_modeled} = \delta^{13}C_{atm} + \epsilon_D \frac{(1 - a\, b\, c_{atm})}{c_{atm}} + \epsilon_C ab. \tag{6}$$

Our key assumption is that any anomalies in $\delta^{13}\mathrm{C_{OM}}$ caused by the earthquake are reflected in additional residuals from predicted values (7). Thus, we regard the model residuals as diagnostic of disturbance, following the disturbance hydrology approach by *Buma and Livneh* [2017]. We assume that all residuals except the ones induced by the earthquake are normally distributed. We then compared the observed postseismic $\delta^{13}\mathrm{C_{OM}}$ with the modeled values to calculate a Residual $\delta^{13}\mathrm{C_{OM}}$-Signal (R$\delta^{13}\mathrm{C}_{OM}$S) - the amount by which the observed $\delta^{13}\mathrm{C_{OM}}$ differed from the modeled in the assumed absence of an earthquake disturbance at each time *t*

$$\mathrm{R}\delta^{13}C_{OM}\mathrm{S} = \delta^{13}\mathrm{C}_{\mathrm{OM}_{\mathrm{observed,t}}} - \delta^{13}\mathrm{C}_{\mathrm{OM}_{\mathrm{predicted,t}}} \tag{7}$$

$\mathrm{R}\delta^{13}\mathrm{C}_{OM}\mathrm{S}$ measures the sensitivity to earthquake disturbance in terms of the deviation from the expected $\delta^{13}\mathrm{C}_{\mathrm{OM}}$ time series. Our modified photosynthesis model is linear (Eq. 6) even without using trend-adjusted CO_2 time series; thus, $\mathrm{R}\delta^{13}\mathrm{C}_{OM}\mathrm{S}$ remains unchanged, though absolute residuals may change. Besides the modified Farquhar model, we calculated $\mathrm{R}\delta^{13}\mathrm{C}_{OM}\mathrm{S}$ for a sinusoidal model (Eq. 8), assuming that both xylem growth and $\delta^{13}\mathrm{C}_{\mathrm{OM}}$ follow a simple seasonal cycle [*King et al.*, 2013]. In both cases, we ran *n* = 10,000 MC models to estimate uncertainties:

$$\delta^{13}\mathrm{C}_{OM\_modeled} = \hat{X}\sin(\omega t + \varphi), \tag{8}$$

where $\hat{X}$ is the amplitude, ω is the angular frequency, and φ is the phase.

We also calculated $\mathrm{R}\delta^{13}\mathrm{C}_{OM}\mathrm{S}$ against the arithmetic mean of all measurements per tree and growing season. This approach is widely used in dendroecology [*Feng*, 1998]. To compare between trees and growing seasons, we standardized all residuals. The residuals of modeled vs. measured lumen area, i.e. Residual Lumen Area Signal (RLAS), was calculated the same way as $\mathrm{R}\delta^{13}\mathrm{C}_{OM}\mathrm{S}$. The increments cover time periods of different lengths depending of the timing of cell growth during the season, i.e. early and late wood. In order to make changes in $\delta^{13}\mathrm{C}_{\mathrm{OM}}$ both comparable during the entire growing season but also to keep the transitions between two subsequent measurements smooth, we estimated daily rates of $\delta^{13}\mathrm{C}_{\mathrm{OM}}$ change with cubic smoothing splines with 10 degrees of freedom, following recommendations by *Cantoni and Hastie* [2001].

3.4. Boosted Regression Trees

We used Boosted regression trees (BRT) from the family of generalized boosted models [*Elith et al.*, 2008; *Hastie et al.*, 2009] to identify environmental controls on $\delta^{13}\mathrm{C}_{\mathrm{OM}}$ and lumen area other than seismic. This step characterizes the main environmental controls of the studied proxies in the absence of a seismic event, and allows for comparison among the tree cohorts and individuals. BRTs are ensembles of decision trees trained on data, forming a nonparametric model capable of handling large nonlinear, noisy, fragmented, or correlated multidimensional data for classification and regression [*Elith et al.*, 2008; *Hastie et al.*, 2009]. BRTs combine two algorithms: (1) regression trees from the decision tree group of models, and (2) boosting to build an ensemble of models. The hierarchical structure of BRTs means that the response to one input variable depends on residuals higher in the tree structure, so that interactions between predictors are automatically modeled. Boosting is a sequential method for improving model accuracy, based on the idea that averaging the output of many poorly skilled models ("weak learners") can offer more accurate predictions ("strong learners") [*Elith et al.*, 2008]. The strategy is to sequentially train tree models on the residuals of their predecessors. Boosting numerically minimizes the loss function by adding, at each step, a new tree that best reduces (or steps down the steepest gradient of) the loss function. Boosting thus focuses on the variation in the response unexplained by the model. *Elith et al.* [2008] pointed out two key features of BRTs:

(1) The model structure is stochastic for improved predictive performance. The variance of the final model is reduced by using only a random subset of data to fit each new tree [*Friedman*, 2002]. Among others, the variance is controlled by defining the bag fraction that specifies the proportion of data to be selected at each step.

(2) The sequential fitting process builds on trees fitted previously, and increasingly focuses on the highest residuals to predict. This distinguishes the process from one where a single large tree is fitted to the data set [Hastie et al., 2009].

The learning rate (*lr*) determines the contribution of each tree to the growing model, and the tree complexity (*tc*) controls whether interactions are fitted. These two parameters then determine the number of trees (*nt*) required for optimal prediction. Decreasing *lr* increases the required *nt*. In general smaller *lr* and larger *nt* are preferable [*Elith et al.*, 2008]. We used the R package gbm [*Greenwell et al.*, 2020] and set the learning rate *lr* = 0.001 and tree complexity *tc*

= 5, resulting in >3,000 trees, following recommendations by *Elith et al.* [2008]; we set the bag fraction to 0.5. The model produces measures of variable importance based on the number of times a variable is selected for splitting, weighted by the squared improvement to the model as a result of each split, and averaged over all trees [*Friedman and Meulman*, 2003]. The relative importance of variables is scaled such that their sum adds to 100, with higher numbers indicating stronger influence on the response. While the variable importance in an BRT model provides an estimate for the predictor importance in non-linear data, thus augmenting a simple correlation matrix showing linear dependence between predictor and response variables. The response variables are $\delta^{13}\mathrm{C_{OM}}$ and mean lumen area (LA), whereas the predictors accounted for antecedent mean solar radiation, mean air temperature, mean streamflow discharge and maximum, mean, and cumulative precipitation. These antecedent conditions are the time windows captured by each single measurement of LA and $\delta^{13}\mathrm{C_{OM}}$ increments. For $\delta^{13}\mathrm{C_{OM}}$ we integrated the data at 100-µm increments, covering periods ranging from days to weeks depending on the time within the growing season. For the wood anatomy, we used the data per tree ring, i.e., integrated over one growing season. Besides the topographic measures (Table 2), our predictors also include tree and site-specific information, i.e., the individual tree and slope position (ridge and valley bottom).

4 Results

4.1 Growth modeling and time of cell differentiation

Our measured field data show a continuous growing season throughout the entire year starting in June (Table S1). Assuming a growing season from June 1 to May 31, and best-fit model parameters $A = 132.0^{+5.03}/_{-4.18}$, $\beta = 1.54^{+0.06}/_{-0.06}$, and $\kappa = 0.009^{+0.001}/_{-0.001}$ $(1/t)$, our Gompertz growth model has an $R^2 = 0.99 \pm 0.001$. The model overestimates accumulated growth during the early growing season, but more accurately fits growth towards the end, when the earthquake occurred (Fig. 4).

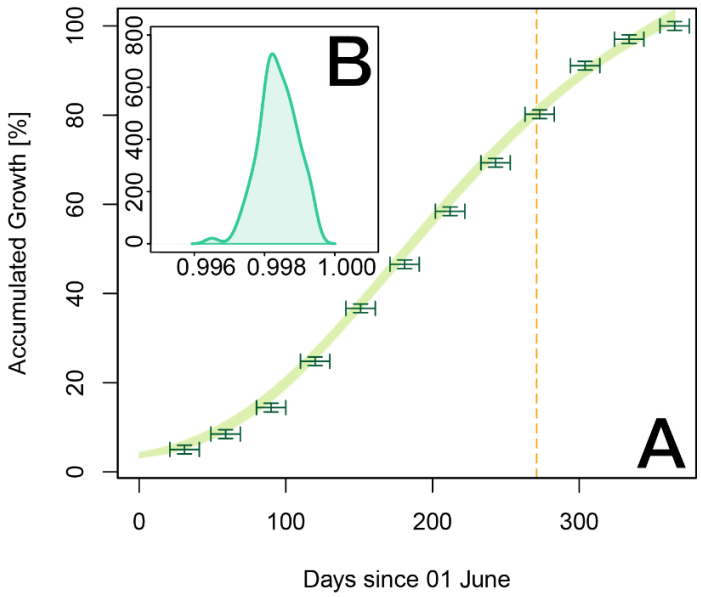

Figure 4. Observed and modeled cumulative tree growth per growing season. **a)** Light green curves are *n* = 10,000 Monte-Carlo (MC) Gompertz model fits to the measured data (dark green). Dark green error bars encompass the measured monthly DBH growth with measurement errors (whiskers). The timing of the earthquake during the growing period is highlighted as the orange dashed line. **b)** Distribution of the model fits (R^2 values) for the 10,000 MC models.

4.2 Wood anatomy

4.2.1 Inter-annual wood anatomy

When averaged over all growing seasons from 2008/2009 to 2012/2013, tree-ring width (4.56 ± 1.71 mm and 2.67 ± 0.88 mm), lumen area (336.7 ± 50.4 μm^2 and 269.0 ± 73.9 μm^2) and absolute early wood lumen area (412.9 ± 52.1 μm^2 and 341.8 ± 64.6 μm^2) on valley floors exceed those on the hillslope ridge ($p \leq 0.01$) (Fig. 5A, C). Yet the percentage of early wood is indistinguishable ($p = 0.57$), with 67.7 ± 9.2% and 64.7 ± 11.1% on the ridge and valley floor, respectively (Fig. 5E).

On the ridge, NacPi25 and NacPi30 follow a similar temporal pattern, with moderate linear correlation ($r = 0.61$ and 0.58) between tree ring width and lumen area (Fig. 5B). In contrast, the correlation among the valley-floor trees is negative ($r = -0.41$ to -0.62), and we note a strong correlation between ring width and number of cells for both NacPi6 and NacPi11 (r =

0.89-0.99, Table S6). Early wood hardly varied with time (Table S6), yet its relative differences are more pronounced (Fig. 5F).

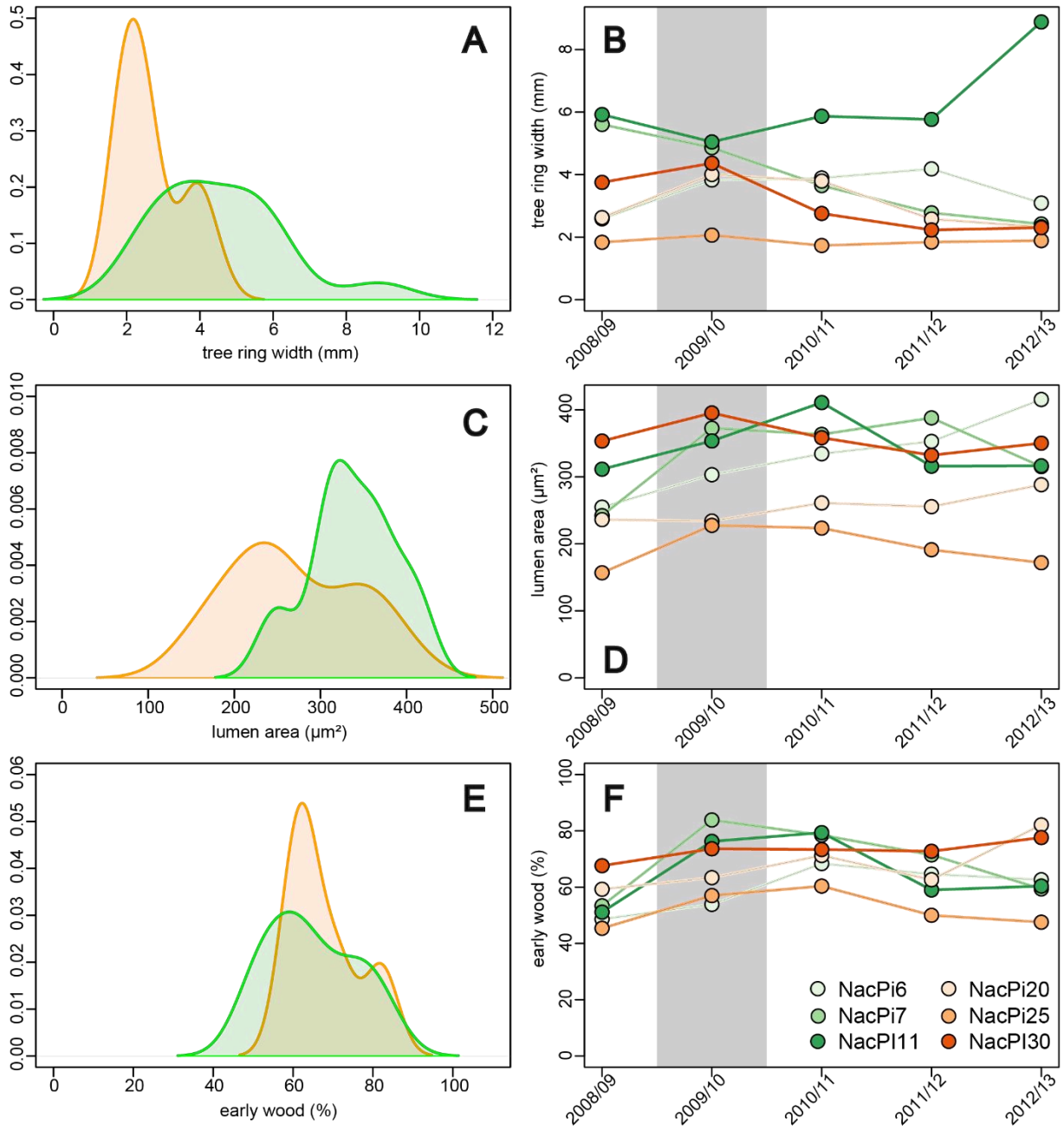

Figure 5. Summary of wood anatomic features. Density curves show (**a**) tree-ring width (mm), (**c**) lumen area (µm^2), and (**e**) percentage of early wood grouped by hillslope ridges and valley bottom. **b, d,** and **f** are the mean wood anatomic features per growing seasons. Red-orange colors

refer to ridge, green to valley floor, respectively. Grey shaded area spans the growing season in which the Maule earthquake happened.

4.3.2 Intra-annual wood anatomy

Our measurements indicate anomalies in lumen area growth in at least two out of six samples, NacPi11 and NacPi25 (Fig. 6C, D). These deviations from the sine model coincide with the timing of the Maule earthquake. NacPi11 indicates a positive deviation, with lumen area increasing from 250 to 390 μm^2, lasting for about one month following the earthquake before returning to the pre-earthquake values (Fig. 6C). The residuals are high compared to NacPi20 and NacPi30 (Fig. S5, Fig. S6), yet within the range of rainstorms in all growing seasons (Fig. S11). Similar increases in lumen area growth also happened in other growing seasons, e.g., 2010-11, tied to rainfall events at the beginning of the growing season (Fig.S3). In contrast, rainfall was scarce in both catchments around the time of the Maule earthquake (Fig. 6A, B). Overall, however, lumen area does not scale with rainfall (Fig. S12B).

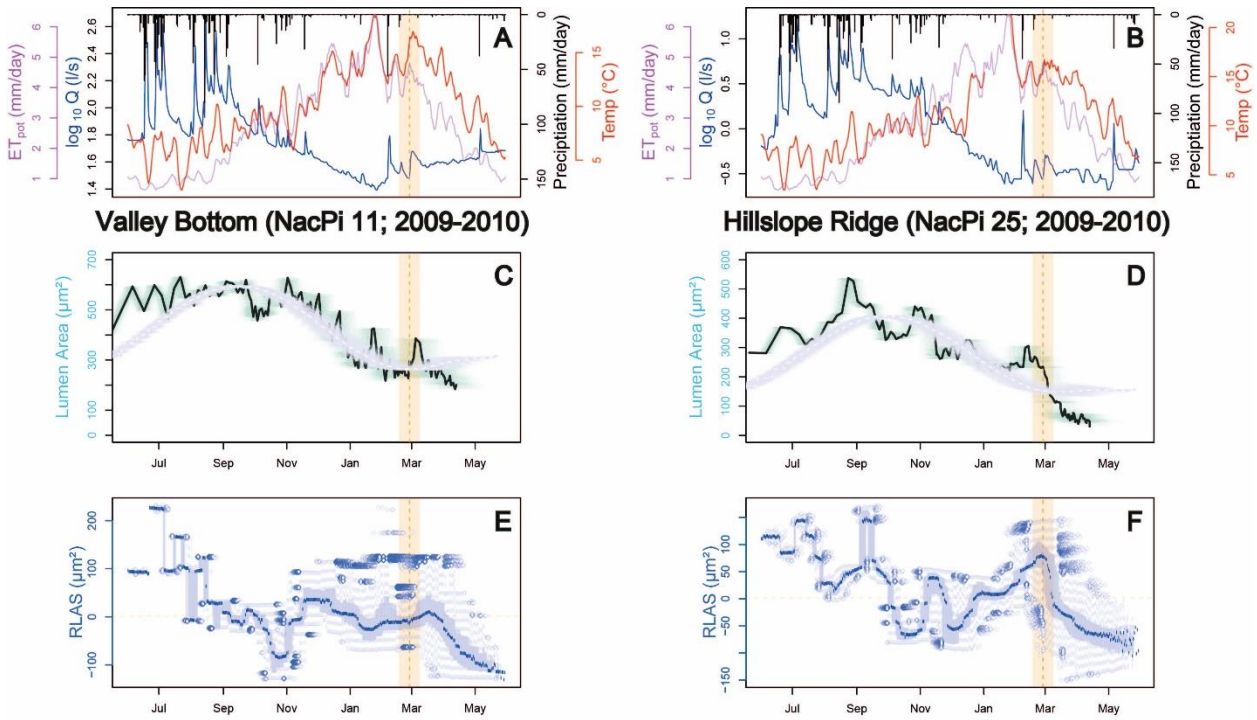

Figure 6. Wood anatomy of sampled trees on the valley floor (NacPi11in **a, c, e**) and the hillslope ridge (NacPi25 in **b, d, e**) for the 2009-10 growing season; streamflow discharge (in logarithmic scale) in blue, rainfall (black), and air temperature (red) for 06/2009-06/2010 measured in Pichún (**a**) and S.A. (**b**); Potential evapotranspiration (red lines) in Nicodahue catchment (#8362001) from the CAMEL-CL dataset [*Alvarez-Garreton et al.*, 2018]. The thick black curves are the medians of n = 10,000 MC-modeled time series of lumen area (green array of curves) and the white dashed lines are the medians of n=10,000 MC sine models from 06/2009 to 05/2010 for NacPi11 (**c**) and NacPi25 (**d**), respectively. The light blue boxplots are the RLAS binned to daily values (**e**, **f**), with the medians in dark blue for NacPi11 (**c**) and NacPi25 (**d**), respectively. The orange bars and dashed lines mark the earthquake date ±10 days.

Trees on the ridge had a decrease in lumen area immediately after the Maule earthquake (Fig. 6D). Lumen area of NacPi25 sharply decreased by 68% from 230 to 65 μm^2 between Feb 25th and March 18th, respectively (Fig. 6D). A similar decrease also occurred in 2011, though stalled after rainfall that prompted increased streamflow (Fig. S4). Both NacPi20 and NacPi30 had similar but smaller decreases (Fig. S5, S6).

4.2 $\delta^{13}C_{OM}$ fractionation

For the period 1991-2012, with -24.89 ± 0.57 ‰ and -25.18 ± 0.72 ‰ , the average $\delta^{13}C_{OM}$ were higher on the ridge compared to the valley floor, respectively (p <0.01, Table S7). During this period, $\delta^{13}C_{OM}$ increased at approx. 0.045 ‰ yr^{-1} for both valley-floor and ridge locations (Fig. S8). Solar radiation was consistently the most important predictor, both on the ridge and the valley bottom (Fig. 7). Accumulated rainfall is more important for $\delta^{13}C_{OM}$ after the earthquake, while temperature is less important after the earthquake. Postseismic streamflow is more important for $\delta^{13}C_{OM}$ on ridges than on the valley bottoms. Neither tree location nor mean or maximum precipitation are particularly important for predicting $\delta^{13}C_{OM}$ (Fig. 7, Table S3).

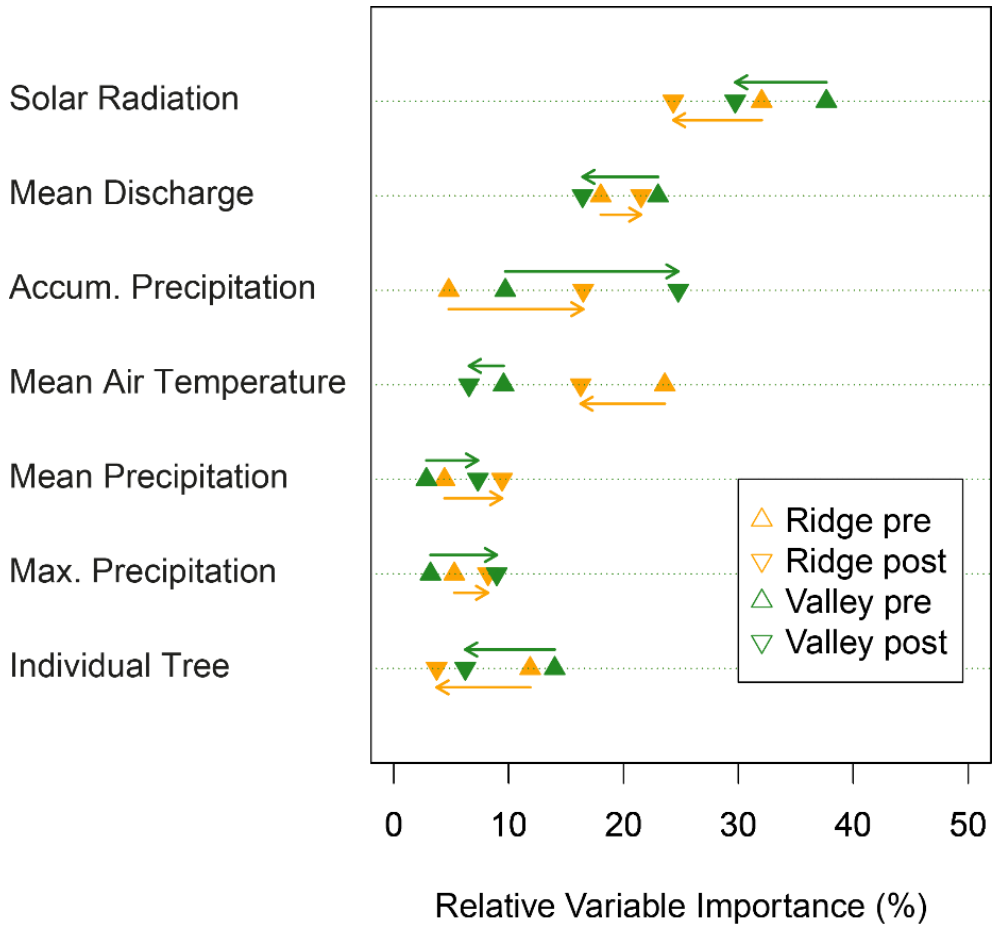

Figure 7. Relative variable importance of Generalized Boosted Regression Models of $\delta^{13}C_{OM}$ for hillslope ridges (orange) and valley floors (green) before and after the earthquake, respectively. The predictors solar radiation, mean temperature, mean discharge, and accumulated maximum and mean precipitation refer to time windows covered by a sample increment and thus cover varying periods; individual tree refers to location. The arrows show changes in variable importance after the earthquake on the ridge (orange) and the valley floor (green). See Supplementary Table 3 for a complete list of relative variable importance and model fits.

A simple correlation exercise reveals additional indications for underlying hydro-environmental controls. In essence, the wetter the site (see, for example, TWI, TPI, normalized height, mean altitude, distance to the next stream, Fig. 8), the higher is $\delta^{13}\mathrm{C_{OM}}$. This scaling also applies for the wood anatomy. For example, TWI is positively correlated with $\delta^{13}\mathrm{C_{OM}}$ (Fig. 8).

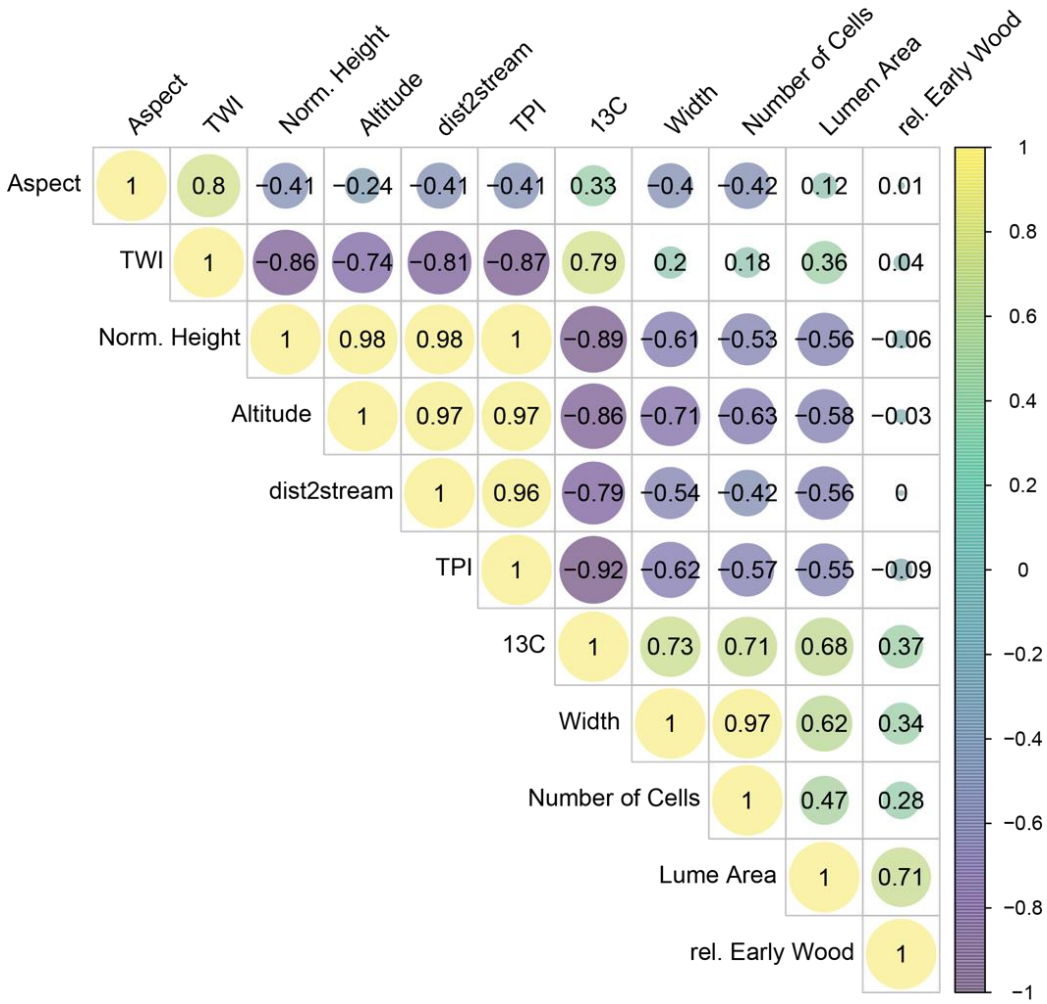

Figure 8. Correlation matrix of environmental conditions of tree growth. Aspect refers to mean aspect (°), TWI is the topographic wetness index, TPI is topographic position index, Altitude is altitude (m asl), all within a 10-m buffer around each tree. Normalized height is dimensionless. dist2stream is the distance of the sampled tree from the nearest stream (m) (Table 2). $\delta^{13}\mathrm{C_{OM}}$ is standardized for each tree, width is mean annual tree-ring width, number of cells refers to the mean along the eight paths, lumen area is to the average and percentage early wood is the mean of early wood in each annual tree ring. The numbers are Pearson correlation coefficients; $r = 1$ between TPI and Norm. Height is due to rounding of r = 0.997.

After the earthquake, the measured $\delta^{13}\mathrm{C_{OM}}$ in NacPi11 decreased faster than our model means, particularly that of the sine model (see **a** in Fig. 9C), as the absolute (negative) model

residuals switched from 0.24 (‰) on Feb 26th to -0.53 (‰) on the day of the earthquake and increased to -1.06 (‰) on March 29th, i.e. for a period of less than five weeks (30 days). A similar increase in residuals is also observed for both alternative modeling approaches; residuals are smallest for the sine model (Fig. 9E). The estimated daily rates of $\delta^{13}\mathrm{C_{OM}}$ largely remained unchanged (Fig. 9C).

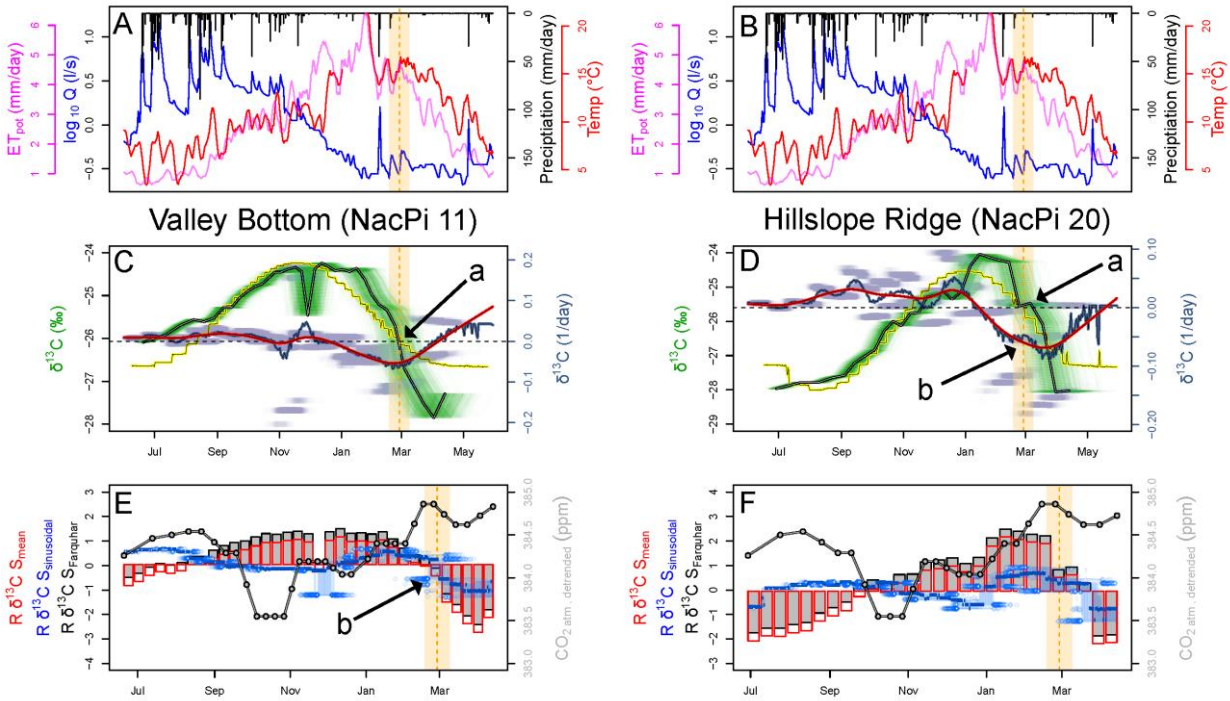

Figure 9. $\delta^{13}\mathrm{C_{OM}}$ fractionation of NacPi11 (left) and NacPi20 (right) in the growing season 2009-2010. A, B: Time series of discharge (on logarithmic scale) in blue, rainfall (black), air temperature (red), and potential evapotranspiration (pink). **a)** Data on streamflow discharge, rainfall, and air temperature from Pichún (**a**) and S.A. (**b**) catchments, respectively; potential evapotranspiration from Nicodahue catchment (#8362001) of CAMEL-CL data [*Alvarez-Garreton et al.*, 2018)]. The orange bars and dashed lines mark the earthquake date ±10 days. **c, d**) The black curve is the median of all MC-modeled time series of $\delta^{13}\mathrm{C_{OM}}$ (n = 10,000, green array of curves) of NacPi11 (**c**) and NacPi20 (**d**). Daily rates of $\delta^{13}\mathrm{C_{OM}}$ change are violet points with violet solid line showing medians and red dashed line showing spline regression. The yellow curves are medians of *n*=10,000 MC- sinusoidal–models per sampled cellulose increments. **e, f**): Residual $\delta^{13}C_{OM}$ signals (R$\delta^{13}C_{OM}$S); grey and red bars are $\delta^{13}\mathrm{C_{OM}}$-residuals

to of the Farquhar-models and residuals between observed $\delta^{13}\mathrm{C_{OM}}$-values and the annual mean, respectively. The blue boxplot time series are daily $\delta^{13}\mathrm{C_{OM}}$-residuals of sinusoidal model. The grey dotted curves are de-trended atmospheric CO_2 (ppm) measured at Baring Head, New Zealand [*Keeling et al.*, 2001].

Measured $\delta^{13}\mathrm{C_{OM}}$ at NacPi20 also decreased from -24.04 (‰) on Jan 15th to the minimum of -27.07 (‰) of March 31st. Amid this trend, a transient increase in the residuals coincides with the timing of the earthquake (**a** inFig. 9D, F). The estimated daily rates of $\delta^{13}\mathrm{C_{OM}}$ remained unchanged (p = 0.31). Around the time of the earthquake, however, the rates fell slower when compared to a simple spline interpolation (**b** in Fig. 9D). This small offset is in line with the observed transiently interrupted trend in $\delta^{13}\mathrm{C_{OM}}$ decline towards the end of the growing season (Fig. 9D). A transient increase in $\delta^{13}\mathrm{C_{OM}}$ is also seen for NacPi30 (Fig. S9), even more pronounced in the model residuals.

5 Discussion

5.1 Site specific and inter-annual patterns of $\delta^{13}\mathrm{C_{OM}}$ and wood anatomy

Tree growth is either energy- or water-limited or a combination of both [*Babst et al.*, 2019]. The growth of *Pinus radiata* in Mediterranean areas such as south-central Chile is generally water-limited [*Ojeda et al.*, 2018], thus following a temporal pattern determined by the water supplied during the rainy season. While previous studies suggest a growing season from September to April [*Álvarez et al.*, 2012], our original field data instead support a longer, year-round season from June to May (Fig. 4), most likely sustained by subsurface water storage capacities. Previous work in the study catchments points to near-saturated conditions of deeper soils (>180 cm) even during summer [*Huber et al.*, 2010; *Mohr et al.*, 2015], thus still providing water for *Pinus radiata* D.Don, likely prolonging the growing season. Factors other than water deficit affect tree growth in pine plantations of southern-central Chile, such as vapor pressure deficit or soil water holding capacity [*Álvarez et al.*, 2012]. Yet, we argue that water availability and soil water saturation are the prime controls for tree growth (and photosynthesis), given the strong correlations between $\delta^{13}\mathrm{C_{OM}}$ and wood anatomic proxies (tree ring width, number of cells, and lumen area) with the topographic wetness index (TWI), absolute and relative altitude,

TPI and distance to streams. Thus, the higher, farther from soil water, and drier a tree site is, the lower the $\delta^{13}\mathrm{C_{OM}}$ and the more restricted is tree growth (Fig. 8). A negative relationship between TPI and tree growth has been reported for various environments [*Bałazy et al.*, 2019; *Jucker et al.*, 2018], likely independent of local hydroclimatic conditions.

In general, we find that all dendro-ecological proxies indicate more favorable conditions for tree growth on the valley floor close to the stream, compared to ridges. This contrast holds if including elevation and discrimination rates of $\delta^{13}\mathrm{C_{OM}}$ for *Pinus radiata* D.Don, 2.53‰ km^{-1} [*Warren et al.*, 2001], as elevation modulates carboxylation capacities and stomatal conductance [*Qiang et al.*, 2003]. A higher irradiance in the valley is unlikely the reason for these site-specific differences for at least two reasons. First, the valley floor and the ridge sites have similar north-facing aspects and indistinguishable tree-height distributions [*Huber et al.*, 2010] and thus receive similar potential incoming solar radiation (Table S5). Second, forests remained undisturbed during the study period, so that we exclude changing shadow effects from neighboring trees. *McCarroll and Loader* [2004] point out that $\delta^{13}\mathrm{C_{OM}}$ may correlate with irradiance following thinning as tree crowns reach higher canopy strata [*Mölder et al*., 2011]. We infer that irradiance patterns insufficiently explain differences in $\delta^{13}\mathrm{C_{OM}}$ between sites nor its increase over time. Instead, the increasing $\delta^{13}\mathrm{C_{OM}}$ between 1991 and 2012 is consistent with an 'age effect' of trees and increasing atmospheric CO_2 concentrations (Fig. S8). Given tree ages of 21 to 26 years at the time of coring [*Huber et al.*, 2010], the trees were at 70-90% of their maximum growth rates [*Cerda Vargas and Nuñez Sandoval*, 1996] (Fig. S7), and likely in the thick of expanding their canopies judging from the increasing $\delta^{13}\mathrm{C_{OM}}$. Also, water-use efficiency increases in response to rising atmospheric CO_2 concentrations [*Gessler et al.*, 2014]. Assuming enhanced water use because of higher atmospheric CO_2 concentrations, we would expect that the residuals of our detrended photosynthesis model increase with time, i.e. the higher the atmospheric CO_2 concentration, the higher the residuals. This is not the case (Fig. S8).

5.2 Intra-annual wood anatomy and $\delta^{13}C_{OM}$

Our observations largely agree with a three-phase $\delta^{13}\mathrm{C_{OM}}$ sequence model proposed for broad-leaf deciduous trees [*Helle and Schleser*, 2004a], as we measured highest $\delta^{13}\mathrm{C_{OM}}$ during periods of highest potential evapotranspiration that coincides with dry and hot summer

conditions and high atmospheric and soil water stress. At the same time, the storage effects may explain the offsets between subsequent growing seasons [*Helle and Schleser*, 2004a]. Assuming a simplified, sinusoidal growing cycle, the $\delta^{13}\mathrm{C_{OM}}$ pattern largely followed the expected seasonal pattern [*Helle and Schleser*, 2004a; *Warren et al.*, 2001] with a maximum during the peak of the dry season, regardless of slope position (Fig. 9C, D). Compared to the averages over the study period, low $\delta^{13}\mathrm{C_{OM}}$ and large wood anatomic features, i.e. tree ring width, number of cells, lumen area, and early wood formation, point to particularly favorable growing conditions during the 2009-2010 growing season regardless of topographic position. We attribute these improved growing conditions to the wetter and more extended rainy season relative to the previous one (Table 1). Our interpretation is similar to that by *Carvalho et al.* [2015], who found a close correlation between soil moisture and lumen diameter for pine under water-limited conditions. Assuming higher-than-average water supply during the 2009-2010 growing season, we expect that increased stomatal aperture and RuBisCO promoted higher rates of photosynthesis [*Helle and Schleser*, 2004b], consistently with a lower $\delta^{13}\mathrm{C_{OM}}$. In contrast, the values for 2008/09 and 2009/2010 might arise from the transition from a La Niña to an El Niño in the Southern Oscillation [*Kim et al.*, 2011]. Our measured $\delta^{13}\mathrm{C_{OM}}$ cross-correlation with the Southern Oscillation Index (SOI) lagged by up to three years (Fig. S10B). El Niño may have provided sufficient water to recharge the water storage given that soils and sediments may exceed depths of >5 m [*Mohr et al.*, 2012]. During the subsequent years, the trees may have been fed by earlier precipitation. These years, in turn, were dominated by the onset of the Central Chile Mega Drought [*Garreaud et al.*, 2020].

5.3 Potential earthquake effects on wood anatomy and $\delta^{13}C_{OM}$

At the beginning of the growing season, tree growth depends on reserves (= early wood), mainly stored as starch during the previous year. Starch accumulates in tissues of the sapwood or the phloem cells during summer and autumn (= latewood). In spring, when the period of fast growth commences, starch is mobilized again and transported from storage to meristematic tissue [*Helle and Schleser*, 2004a]. The offsets between two successive growing seasons (Fig. S9) and the resulting misfit of some sine models mainly during early wood formation, may reflect such storage effects causing abrupt steps in isotopic ratios. However, a $\delta^{13}\mathrm{C_{OM}}$-storage

effect may not explain the post-seismic steps because storage effects may only affect early wood but not latewood. The Maule earthquake occurred during latewood formation.

Given the warm and drought conditions in summer 2010, we can assume narrow stomatal apertures and a slow decline of $\delta^{13}\mathrm{C_{OM}}$ in the latewood of the 2009-2010 growing cycle. On the valley floor, the decrease in $\delta^{13}\mathrm{C_{OM}}$ is faster than the modeled values (Fig. 9C), thus suggesting enhanced photosynthesis. In contrast, an abrupt, short-lived increase in $\delta^{13}\mathrm{C_{OM}}$ at higher elevations (Fig. 9C,D) implies more restricted photosynthesis and unfavorable growing conditions [*Helle and Schleser*, 2004b]. The offset between the estimated daily rates of $\delta^{13}\mathrm{C_{OM}}$ and the spline-interpolated is, despite being small, 'significant' and in line with this interpretation. Because $\delta^{13}\mathrm{C_{OM}}$ negatively scales with relative soil water [*Dupouey et al.*, 1993], we explain these different responses with differences in soil-water availability following the seismic shock. Higher and lower soil moisture along the valley floor (= discharge area) and ridge (= recharge area), respectively, are consistent with modeled streamflow responses to the Maule earthquake [*Mohr et al.*, 2015]. Our wood anatomical results are in good agreement with this interpretation. Under the water-limited Mediterranean climate, pine trees can plastically adjust their tracheid sizes to soil-water content. While enlarging the tracheids, water can only enter the expanding cell if the apoplastic water potential is higher than the symplastic water potential [*Carvalho et al.*, 2015]. We can exclude that rainfall raised the soil moisture on the valley floor, because conditions for several days prior to the earthquake were dry. Further, the sites are close together, have similar aspect, and thus likely receive similar amounts of rainfall.

Altogether, our observations are consistent with enhanced and reduced evapotranspiration on the valley bottom and ridge areas, respectively, caused by earthquake-triggered changes in soil-water availability. At a first glance, this finding is counter-intuitive as it suggests possible positive effects of earthquakes on tree growth as opposed to the many reports of negative effects on tree growth [e.g., *Fu et al.*, 2020; *Lin and Lin*, 1998; *Meisling and Sieh*, 1980]. Yet our contrasting responses between the valley floor and the hillslope ridge are consistent with reports by *Bekker et al.* [2018]. These authors found that tree rings were broader in a riparian zone compared to higher areas, likely driven by a rise in groundwater after the M6.9 1983 Borah Peak earthquake, Idaho. The peak ground velocity of >50-25 cm/s was similar for both the Borah and Maule earthquakes [*Mohr et al.*, 2018, *U.S. Geological Survey*, 2021).

We emphasize that not all trees share a site-specific response. The dendro-ecologic response on the hillslope ridge seems more uniform compared to the valley bottom (e.g., Fig. 5B). We explain this contrast with the groundwater topography. The local groundwater depth is greater at higher topographic positions because the unconfined groundwater surface does not follow the surface topography. Hence, seismogenic lowering of the groundwater table may only slightly reduce water availability further, as the soils were aleady extemely dry. Along the valley bottom, instead, even a small additional supply of water may make a difference, thus stimulating tree growth given severe water deficits. As the subsurface is heterogeneous in soil hydrological terms with subsurface flow paths and soil hydrologic properties disturbed by previous rotations [*Mohr et al.*, 2013], we cannot expect consistent seismo-hydrological responses. Some further possibilities for the variable tree growth responses to the Maule earthquake include death of neighboring trees due to forest management, wind throw [*Buma and Johnson*, 2015], or root damage by ground shaking [e.g., *Lin and Lin*, 1998; *Meisling and Sieh*, 1980; *Spiecker*, 2003]. However, we could not find any field evidence for any of these anomalies.

The overall, relative effects of the Maule earthquake on wood isotopic fractionation and tree growth are small. For the valley bottom, the responses in $\delta^{13}\mathrm{C_{OM}}$ and lumen area do not exceed the 0.78 and <0.83 quantiles. Along the hillslope ridges, these responses are as small as the 0.13 quantiles for $\delta^{13}\mathrm{C_{OM}}$ and <0.95 for the lumen area, respectively (Fig. S11, Table S8). Hence, single major rainstorms may have larger impact on the dendroecology in these forest stands and, given the data available, we can only speculate about potential ecohydrological and ecogeomorphic effects of the site-specific, contrasting dendroecological responses reported here. For example, a short-term positive earthquake effect on plant growth may potentially increase root cohesion immediately after the earthquake in lower elevation areas, as suggested by *Tolorza et al*. [2019], and the seismic shaking may also directly or indirectly - via higher soil-water content [*Sidle and Ochiai*, 2006] - surpass or counteract this change in cohesion.

The Gompertz growth model is needed to assign dates to our samples, because neither wood anatomic features nor intra-annual $\delta^{13}\mathrm{C_{OM}}$ sample increments reveal information about events such as the Maule earthquake or rainstorms. Tree growth is a non-linear process [e.g., *Fekedulegn and Colbert*, 1999]. We note that uncertainties in our dating procedure propagate trough time, such that they increase towards the end of the growing season, culminating when

the Maule earthquake occurred. This was a time when latewood formation reduced the temporal resolution because of a lower tracheid formation rate [*Carvalho et al.*, 2015]. While the total uncertainty is hard to quantify, we consider an interval of 21 days to be suitable as it covers periods longer than a single cell needs to grow even at the end of the growing season. Thus, we are confident that our dating allows for a scientifically sound interpretation.

We are aware that assuming a linear relationship between the leaf intercellular CO_2 concentrations and ambient atmospheric CO_2 concentration, that in turn feeds into the Farquhar photosynthesis model, is simplified. Leaf intercellular CO_2 concentrations vary during a growing season [*Gessler et al.*, 2014] following changes in temperature, and water vapor effects on stomata conductance and diffusivity [*Tominaga et al.*, 2018]. However, *Moss and Rawlins* [1963] reported a linear relationship with values close to our estimates. When comparing the residuals, our modified photosynthesis model performs (slightly) better than a simple, commonly applied approach of normalizing $\delta^{13}\mathrm{C_{OM}}$ measurements [*Feng*, 1998]. This supports the use of our modified Farquhar model with a sinusoidal trend to predict $\delta^{13}\mathrm{C_{OM}}$ values with acceptable uncertainties.

We argue that water stress around the time of an earthquake is required to record hydrological effects of earthquakes in tree rings. Only under water-limited tree growth, as in the case here [*Ojeda et al.*, 2018], will additional water provided by seismo-hydrological processes lead to enhanced root water uptake and eventually measureable changes in tree growth and photosynthetic activity. Future research may want to examine the possibility of similar responses in other settings with prolonged dry seasons. Good candidates to test our hypothesis are earthquakes in California, e.g., 2014 M6.6 South Napa or 1989 M6.9 Loma Prieta, [*Rojstaczer and Wolf*, 1992; *Wang and Manga*, 2015], whereas the best studied earthquakes in terms of hydrological phenomena, the 1999 M7.7 Chi-Chi Earthquake in Taiwan [e.g., *Wang et al.*, 2016; *Wang et al.*, 2004], is unlikely to be a promising candidate because of the tropical climate.

5 Conclusions

The Maule earthquake had an influence on tree growth in the studied catchment but is only discernable over weeks. The common dendrochronological practice restricted to the annual scale may therefore miss earthquakes or underestimate the area affected by a given earthquake.

Our wood anatomy and biogeochemical data indicate that:

1) Post-seismic changes in lumen area and $\delta^{13}\mathrm{C_{OM}}$ reveal tree growth and photosynthetic responses to earthquakes; however, such responses likely only apply under water-limited conditions, i.e. when earthquakes are capable to relief water stress by providing additional water to the plants. These circumstances need to be considered in sampling campaigns when considering tree coring in paleoseismology.

2) The recorded response of tree growth to the Maule earthquake depended on the locations of the tree in the catchment, with enhanced growth along the valley floor but decreased growth along the ridges.

Lastly, our observed earthquake signals show in changes in $\delta^{13}\mathrm{C_{OM}}$ and wood anatomical features, and lasted less than a year, unlike the longer-lived perturbation to tree growth documented in other studies based on tree-ring widths. Details in wood anatomy and isotopes might offer a tree-based approach for paleoseismology beyond simply considering width. Recognizing the subtle signals in the studied trees, however, benefitted from known climatology, plausible parameterization of photosynthesis-models, and precipitation and temperature records.

Acknowledgments, Samples, and Data

We appreciate funding by project US National Science Foundation 1344424 awarded to M.M.. C.H.M and O.K received funding from the German Federal Ministry of Education and Research (01DN13060) and the Potsdam Graduate School. Jenny Tamm, Debora Bodewitz and Johannes Schnell helped with laboratory analyses. We ran all computations using the statistical environment R. We thank Oscar Maradones and Forestal Minico for providing access to the catchments, the measured tree growth data, and the permission to core the trees. The datasets for this research are included in this paper and its supplementary information files. We are going to upload the data to hydroshare, pending the final decision on this manuscript.

References

Allen, R. B., D. I. MacKenzie, P. J. Bellingham, S. K. Wiser, E. A. Arnst, D. A. Coomes, and J. M. Hurst (2020), Tree survival and growth responses in the aftermath of a strong earthquake, *J. Ecol.*, 108(1), 107-121, doi:10.1111/1365-2745.13238.

Alvarez-Garreton, C., et al. (2018), The CAMELS-CL dataset: catchment attributes and meteorology for large sample studies – Chile dataset, *Hydrol. Earth Syst. Sci. Discuss.*, 2018, 1-40, doi:10.5194/hess-2018-23.

Álvarez, J., H. L. Allen, T. J. Albaugh, J. L. Stape, B. P. Bullock, and C. Song (2012), Factors influencing the growth of radiata pine plantations in Chile, *Forestry*, 86(1), 13-26, doi:10.1093/forestry/cps072.

Arsdale, R. B. V., D. W. Stahle, M. K. Cleaveland, and M. J. Guccione (1998), Earthquake signals in tree-ring data from the New Madrid seismic zone and implications for paleoseismicity, *Geology*, 26(6), 515-518, doi:10.1130/0091-7613(1998)026<0515:esitrd>2.3.co;2.

Atwater, B. F., and D. K. Yamaguchi (1991), Sudden, probably coseismic submergence of Holocene trees and grass in coastal Washington State, *Geology*, 19(7), 706-709, doi:10.1130/0091-7613(1991)019<0706:spcsoh>2.3.co;2.

Babst, F., O. Bouriaud, B. Poulter, V. Trouet, M. P. Girardin, and D. C. Frank (2019), Twentieth century redistribution in climatic drivers of global tree growth, *Sci. Adv.*, 5(1), eaat4313, doi:10.1126/sciadv.aat4313.

Bałazy, R., A. Kamińska, M. Ciesielski, J. Socha, and M. Pierzchalski (2019), Modeling the Effect of Environmental and Topographic Variables Affecting the Height Increment of Norway Spruce Stands in Mountainous Conditions with the Use of LiDAR Data, *Remote Sens.*, 11(20).

Barrientos, G., A. Herrero, A. Iroumé, O. Mardones, and R. J. Batalla (2020), Modelling the Effects of Changes in Forest Cover and Climate on Hydrology of Headwater Catchments in South-Central Chile, *Water*, 12, 1828, doi:10.3390/w12061828.

Bekker, M., D. P. Metcalf, and G. Harley (2018), Hydrology and Hillslope Processes Explain Spatial Variation in Tree-Ring Responses to the 1983 Earthquake at Borah Peak, Idaho, USA, 3074-3085 pp., doi:10.1002/esp.4470.

Bekker, M. F. (2004), Spatial variation in the response of tree rings to normal faulting during the Hebgen Lake Earthquake, Southwestern Montana, USA, *Dendrochronologia*, 22(1), 53-59, doi:https://doi.org/10.1016/j.dendro.2004.09.001.

Beven, K. J., and M. J. Kirkby (1979), A physically based, variable contributing area model of basin hydrology / Un modèle à base physique de zone d'appel variable de l'hydrologie du bassin versant, *Hydrol. Sci. Bull*., 24(1), 43-69, doi:10.1080/02626667909491834.

Boehner, J., R. Koethe, O. Conrad, J. Gross, A. Ringeler, and T. Selige (2002), Soil Regionalisation by Means of Terrain Analysis and Process ParameterisationRep., 213-222 pp, European Soil Bureau, Luxemburg.

Boehner, J., Selige, T. (2006), Spatial prediction of soil attributes using terrain analysis and climate regionalisation, in SAGA - Analysis and Modelling Applications, edited by J. Boehner, McCloy, K.R., Strobl, J., pp. 13-28.

Boehner, J., and O. Antonić (2009), Chapter 8 Land-Surface Parameters Specific to Topo-Climatology, in Developments in Soil Science, edited by T. Hengl and H. I. Reuter, pp. 195-226, Elsevier, doi:https://doi.org/10.1016/S0166-2481(08)00008-1.

Breen, S. J., Z. Zhang, and C.-Y. Wang (2020), Shaking Water Out of Sands: An Experimental Study, *Water Res. Res*., 56(10), e2020WR028153, doi:10.1029/2020wr028153.

Buma, B., and A. C. Johnson (2015), The role of windstorm exposure and yellow cedar decline on landslide susceptibility in southeast Alaskan temperate rainforests, *Geomorph*., 228, 504-511, doi:https://doi.org/10.1016/j.geomorph.2014.10.014.

Buma, B., and B. Livneh (2017), Key landscape and biotic indicators of watersheds sensitivity to forest disturbance identified using remote sensing and historical hydrography data, *Environ. Res. Let.*, 12(7), 074028, doi:10.1088/1748-9326/aa7091.

Cantoni, E., and T. Hastie (2001), Degrees of Freedom Tests for Smoothing Splines, *Biometrika*, 89, doi:10.1093/biomet/89.2.251.

Carvalho, A., C. Nabais, J. Vieira, S. Rossi, and F. Campelo (2015), Plastic Response of Tracheids in Pinus pinaster in a Water-Limited Environment: Adjusting Lumen Size instead of Wall Thickness, *PLOS ONE*, 10(8), e0136305, doi:10.1371/journal.pone.0136305.

Cerda Vargas, I., and R. Nuñez Sandoval (1996), Appreciation of the Chilean forest resource: Plantations of Pinus radiata and Eucalyptus sp. 1985-1996, Report FAO, Rome.

Conrad, O., B. Bechtel, M. Bock, H. Dietrich, E. Fischer, L. Gerlitz, J. Wehberg, V. Wichmann, and J. Boehner (2015), System for Automated Geoscientific Analyses (SAGA) v. 2.1.4, *Geosci. Model Dev.*, 8(7), 1991-2007, doi:10.5194/gmd-8-1991-2015.

de la Cruz, M., and L. De Soto (2017), Package 'tgram', edited, pp. Functions to compute and plot tracheidograms, as in De Soto et al. (2011) <doi:2010.1139/x2011-2045>.

Drew, D., and G. Downes (2018), Growth at the microscale: long term thinning effects on patterns and timing of intra-annual stem increment in radiata pine, *For. Ecosys*., 5, doi:10.1186/s40663-018-0153-z.

Du, S., and F. Yamamoto (2007), An Overview of the Biology of Reaction Wood Formation, *J. Integr.Plant Biol.*, 49(2), 131-143, doi:10.1111/j.1744-7909.2007.00427.x.

Dupouey, J.-L., S. Leavitt, E. Choisnel, and S. Jourdain (1993), Modelling carbon isotope fractionation in tree rings based on effective evapotranspiration and soil water status, Plant, *Cell & Environ.*, 16(8), 939-947, doi:10.1111/j.1365-3040.1993.tb00517.x.

Elith, J., J. R. Leathwick, and T. Hastie (2008), A working guide to boosted regression trees, *J. Ani. Ecol.*, 77(4), 802-813, doi:10.1111/j.1365-2656.2008.01390.x.

Elkhoury, J. E., E. E. Brodsky, and D. C. Agnew (2006), Seismic waves increase permeability, *Nature*, 441(7097), 1135-1138.

Farquhar, G. D., S. von Caemmerer, and J. A. Berry (1980), A biochemical model of photosynthetic CO_2 assimilation in leaves of C3 species, *Planta*, 149(1), 78-90, doi:10.1007/BF00386231.

Fekedulegn, D., and J. Colbert (1999), Parameter Estimation of Nonlinear Growth Models in Forestry, *Silva Fennica*, 33, doi:10.14214/sf.653.

Feng, X. (1998), Long-term ci/ca response of trees in western North America to atmospheric CO_2 concentration derived from carbon isotope chronologies, *Oecol*., 117(1), 19-25, doi:10.1007/s004420050626.

Friedman, J. H. (2002), Stochastic gradient boosting, *Comput. Stat. Data Anal.*, 38(4), 367–378, doi:10.1016/s0167-9473(01)00065-2.

Friedman, J. H., and J. J. Meulman (2003), Multiple additive regression trees with application in epidemiology, *Statistics in medicine*, 22(9), 1365-1381, doi:10.1002/sim.1501.

Fu, T., E. Liang, X. Lu, S. Gao, L. Zhang, H. Zhu, S. Rossi, and J. Julio Camarero (2020), Tree growth responses and resilience after the 1950-Zayu-Medog earthquake, southeast Tibetan Plateau, *Dendrochronologia*, 62, 125724, doi:https://doi.org/10.1016/j.dendro.2020.125724.

Galle, A., J. Esper, U. Feller, M. Ribas-Carbo, and P. Fonti (2010), Responses of wood anatomy and carbon isotope composition of Quercus pubescens saplings subjected to two consecutive years of summer drought, *Ann. For. Sci.*, 67(8), 809-809, doi:10.1051/forest/2010045.

Garreaud, R. D., J. P. Boisier, R. Rondanelli, A. Montecinos, H. H. Sepúlveda, and D. Veloso-Aguila (2020), The Central Chile Mega Drought (2010–2018): A climate dynamics perspective, *Inter. J. Climatol.*, 40(1), 421-439, doi:https://doi.org/10.1002/joc.6219.

Gessler, A., J. P. Ferrio, R. Hommel, K. Treydte, R. A. Werner, and R. K. Monson (2014), Stable isotopes in tree rings: towards a mechanistic understanding of isotope fractionation and mixing processes from the leaves to the wood, *Tree Physiol.*, 34(8), 796-818, doi:10.1093/treephys/tpu040.

Greenwell, B., B. Boehmke, and J. Cunningham (2020), gbm: Generalized Boosted Regression Models, edited.

Hargreaves, G. H., and A. Z. Samani (1985), Reference Crop Evapotranspiration from Temperature, *Applied Engin. Agricul.*, 1(2), 96-99, doi:https://doi.org/10.13031/2013.26773.

Hastie, T., R. Tibshirani, and J. Freidman (2009), The elements of statistical learning - Data mining, inference, and prediction., New York.

Helle, G., and G. H. Schleser (2004a), Beyond CO_2-fixation by Rubisco – an interpretation of $^{13}C/^{12}C$ variations in tree rings from novel intra-seasonal studies on broad-leaf trees, *Plant, Cell & Environ.*, 27(3), 367-380, doi:10.1111/j.0016-8025.2003.01159.x.

Helle, G., and G. H. Schleser (2004b), Interpreting climate proxies from tree-rings, in Towards a synthesis of Holocene proxy data and climate models, edited by H. Fischer, G. Floeser, T.

Kumke, G. Lohmann, H. Miller, J. F. W. Negendank and H. von Storch, pp. 124-137, Springer, Berlin.

Holmes, R. (1983), Computer-Assisted Quality Control in Tree-Ring Dating and Measurement.

Huber, A., A. Iroumé, C. H. Mohr, and C. Frene (2010), Effect of Pinus radiata and Eucalyptus globulus plantations on water resource in the Coastal Range of Biobio region, Chile, *Bosque*, 31(3), 219-230.

Jacoby, G. C. (1997), Application of tree ring analysis to paleoseismology, *Rev. Geophys.*, 35(2), 109-124, doi:10.1029/96rg03526.

Jacoby, G. C., D. E. Bunker, and B. E. Benson (1997), Tree-ring evidence for an A.D. 1700 Cascadia earthquake in Washington and northern Oregon, *Geology*, 25(11), 999-1002, doi:10.1130/0091-7613(1997)025<0999:trefaa>2.3.co;2.

Jacoby, G. C., P. R. Sheppard, and K. E. Sieh (1988), Irregular Recurrence of Large Earthquakes Along the San Andreas Fault: Evidence from Trees, *Science*, 241(4862), 196-199, doi:10.1126/science.241.4862.196.

Jucker, T., B. Bongalov, D. F. R. P. Burslem, R. Nilus, M. Dalponte, S. L. Lewis, O. L. Phillips, L. Qie, and D. A. Coomes (2018), Topography shapes the structure, composition and function of tropical forest landscapes, *Ecol. Let.*, 21(7), 989-1000, doi:10.1111/ele.12964.

Keeling, C. D., S. C. Piper, R. B. Bacastow, M. Wahlen, T. P. Whorf, M. Heimann, and H. A. Meijer (2001), Exchanges of atmospheric CO_2 and $^{13}CO_2$ with the terrestrial biosphere and oceans from 1978 to 2000, edited by S. I. o. Oceanography, San Diego.

Keeling, C. D., and T. P. Whorf (2004), Atmospheric Carbon Dioxide Concentrations at 10 Locations Spanning Latitudes 82°N to 90°SRep., 33 pp, Scripps Institution of Oceanography, La Jolla, California 92092-0244.

Keeling, R. F., H. D. Graven, L. R. Welp, L. Resplandy, J. Bi, S. C. Piper, Y. Sun, A. Bollenbacher, and H. A. J. Meijer (2017), Atmospheric evidence for a global secular increase in carbon isotopic discrimination of land photosynthesis, *PNAS*, 114(39), 10361-10366, doi:10.1073/pnas.1619240114.

Kim, D., Y.-S. Jang, D.-H. Kim, Y.-H. Kim, M. Watanabe, F.-F. Jin, and J.-S. Kug (2011), El Niño–Southern Oscillation sensitivity to cumulus entrainment in a coupled general circulation model, *J. Geophys. Res. Atmos.*, 116(D22), doi:10.1029/2011jd016526.

King, G., P. Fonti, D. Nievergelt, U. Büntgen, and D. Frank (2013), Climatic drivers of hourly to yearly tree radius variations along a 6 ◦C natural warming gradient, *Agricul. For. Meteorol.*, 168, 36-46, doi:10.1016/j.agrformet.2012.08.002.

Kitzberger, T., T. T. Veblen, and R. Villalba (1995), Tectonic influences on tree growth in northern Patagonia, Argentina: the roles of substrate stability and climatic variation, *Can. J. For. Res.*, 25(10), 1684-1696, doi:10.1139/x95-182.

Leavitt, S. W. (2010), Tree-ring C–H–O isotope variability and sampling, *Sci. Total Environ.*, 408(22), 5244-5253, doi:https://doi.org/10.1016/j.scitotenv.2010.07.057.

Liang, W., I. Heinrich, G. Helle, I. D. Liñán, and T. Heinken (2013), Applying CLSM to increment core surfaces for histometric analyses: A novel advance in quantitative wood anatomy, *Dendrochronologia*, 31(2), 140-145, doi:http://dx.doi.org/10.1016/j.dendro.2012.09.002.

Lin, C. W., and C. W. Lin (1998), Tree damage and surface displacement - the 1931 M 8.0 Fuyun earthquake, *J. Geol.*, 106, 751-757.

Loader, N. J., I. Robertson, A. C. Barker, V. R. Switsur, and J. S. Waterhouse (1997), An improved technique for the batch processing of small wholewood samples to α-cellulose, *Chem. Geol.*, 136(3), 313-317, doi:https://doi.org/10.1016/S0009-2541(96)00133-7.

Ludwig, L.G. (2015), 4.21 - Paleoseismology, in Treatise on Geophysics (Second Edition), edited by G. Schubert, pp. 559-579, Elsevier, Oxford, doi:https://doi.org/10.1016/B978-0-444-53802-4.00088-9.

Lyell, C. (1849), A second visit to the United States of North America, John Murray, London.

Manga, M. (2001), Origin of postseismic streamflow changes inferred from baseflow recession and magnitude-distance relations, *Geophys. Res. Let.*, 28(10), 2133-2136.

Manga, M., E. E. Brodsky, and M. Boone (2003), Response of streamflow to multiple earthquakes, *Geophys. Res. Let.*, 30(5), 1214.

Manga, M., and C. Y. Wang (2015), 4.12 - Earthquake Hydrology, in Treatise on Geophysics (Second Edition), edited by G. Schubert, pp. 305-328, Elsevier, Oxford, doi:http://dx.doi.org/10.1016/B978-0-444-53802-4.00082-8.

McCarroll, D., and N. J. Loader (2004), Stable isotopes in tree rings, *Quat. Sci. Rev.*, 23(7-8), 771-801, doi:10.1016/j.quascirev.2003.06.017.

Meisling, K. E., and K. E. Sieh (1980), Disturbance of trees by the 1857 Fort Tejon Earthquake, California, *J. Geophys. Res. Solid Earth*, 85(B6), 3225-3238, doi:10.1029/JB085iB06p03225.

Mohr, C. H., R. Coppus, A. Iroumé, A. Huber, and A. Bronstert (2013), Runoff generation and soil erosion processes after clear cutting, *J. Geophys. Res. Earth Surf.*, 118(2), 814-831, doi:10.1002/jgrf.20047.

Mohr, C. H., M. Manga, and D. Wald (2018), Stronger Peak Ground Motion, Beyond the Threshold to Initiate a Response, Does Not Lead to Larger Stream Discharge Responses to Earthquakes, *Geophys. Res. Let.*, 45(13), 6523-6531, doi:doi:10.1029/2018GL078621.

Mohr, C. H., M. Manga, C.-y. Wang, J. W. Kirchner, and A. Bronstert (2015), Shaking water out of soil, *Geology*, 43(3), 207-210, doi:10.1130/g36261.1.

Mohr, C. H., M. Manga, C.-Y. Wang, and O. Korup (2017), Regional changes in streamflow after a megathrust earthquake, *Earth Planet. Sci. Let.*, 458, 418-428, doi:http://dx.doi.org/10.1016/j.epsl.2016.11.013.

Mohr, C. H., D. R. Montgomery, A. Huber, A. Bronstert, and A. Iroumé (2012), Streamflow response in small upland catchments in the Chilean coastal range to the M-W 8.8 Maule earthquake on 27 February 2010, *J. Geophys. Res. Earth Surf.*,, 117.

Mohr, C. H., A. Zimmermann, O. Korup, A. Iroumé, T. Francke, and A. Bronstert (2014), Seasonal logging, process response, and geomorphic work, *Earth Surf. Dynam.*, 2(1), 117-125, doi:10.5194/esurf-2-117-2014.

Mölder, I., C. Leuschner, and H. H. Leuschner (2011), $\delta^{13}C$ signature of tree rings and radial increment of Fagus sylvatica trees as dependent on tree neighborhood and climate, *Trees*, 25(2), 215-229, doi:10.1007/s00468-010-0499-5.

Montgomery, D. R., and M. Manga (2003), Streamflow and water well responses to earthquakes, *Science*, 300(5628), 2047-2049.

Moreno, M., M. Rosenau, and O. Oncken (2010), 2010 Maule earthquake slip correlates with pre-seismic locking of Andean subduction zone, *Nature*, 467(7312), 198-U184.

Moss, D. N., and S. L. Rawlins (1963), Concentration of Carbon Dioxide inside Leaves, *Nature*, 197(4874), 1320-1321, doi:10.1038/1971320a0.

Muir-Wood, R., and G. C. P. King (1993), Hydrological Signatures of Earthquake Strain, *J. Geophys. Res. Solid Earth*, 98(B12), 22035-22068.

Nur, A. (2007), 4.22 - Historical Seismicity: Archaeoseismology, in Treatise on Geophysics (Second Edition), edited by G. Schubert, pp. 581-592, Elsevier, Oxford, doi:https://doi.org/10.1016/B978-0-444-53802-4.00089-0.

O'Leary, M. (1988), Carbon Isotopes in Photosynthesis, Biosci., 38(5), 328-336, doi: 10.2307/1310735.

Ojeda, H., R. A. Rubilar, C. Montes, J. Cancino, and M. Espinosa (2018), Leaf area and growth of Chilean radiata pine plantations after thinning across a water stress gradient, New Zealand *J. For. Sci.*, 48(1), 10, doi:10.1186/s40490-018-0116-8.

Page, R. (1970), Dating episodes of faulting from tree rings – Effects of 1958 Rupture of Fairweather Fault on tree growth, *Geol. Soc. Am. Bull.*, 81(10), 3085-&, doi:10.1130/0016-7606(1970)81[3085:deofft]2.0.co;2.

Peel, M. C., B. L. Finlayson, and T. A. McMahon (2007), Updated world map of the Köppen-Geiger climate classification, *Hydrol. Earth Syst. Sci.*, 11(5), 1633-1644, doi:10.5194/hess-11-1633-2007.

R Core Team (2020), R: A language and environment for statistical computing. R Foundation for Statistical Computing, Vienna, Austria.

Reynolds-Henne, C. E., R. T. W. Siegwolf, K. S. Treydte, J. Esper, S. Henne, and M. Saurer (2007), Temporal stability of climate-isotope relationships in tree rings of oak and pine (Ticino, Switzerland), *Glob. Biogeochem. Cycl.*, 21(4), doi:10.1029/2007gb002945.

Rojstaczer, S., and S. Wolf (1992), Permeability Changes Associated With Large Earthquakes - An Example From Loma-prieta, California, *Geology*, 20(3), 211-214.

Rojstaczer, S., S. Wolf, and R. Michel (1995), Permeability Enhancement In the Shallow Crust As A Cause of Earthquake-induced Hydrological Changes, *Nature*, 373(6511), 237-239.

Rossi, S., A. Deslauriers, and H. Morin (2003), Application of the Gompertz equation for the study of xylem cell development, *Dendrochronologia*, 21(1), 33-39, doi:https://doi.org/10.1078/1125-7865-00034.

Schollaen, K., H. Baschek, I. Heinrich, and G. Helle (2015), Technical Note: An improved guideline for rapid and precise sample preparation of tree-ring stable isotope analysis, *Biogeosci. Discuss.*, 2015, 11587-11623, doi:10.5194/bgd-12-11587-2015.

Schollaen, K., H. Baschek, I. Heinrich, F. Slotta, M. Pauly, and G. Helle (2017), A guideline for sample preparation in modern tree-ring stable isotope research, *Dendrochronologia*, 44, 133-145, doi:https://doi.org/10.1016/j.dendro.2017.05.002.

Seo, J.-W., M. Smiljanić, and M. Wilmking (2014), Optimizing cell-anatomical chronologies of Scots pine by stepwise increasing the number of radial tracheid rows included—Case study based on three Scandinavian sites, *Dendrochronologia*, 32(3), 205-209, doi:https://doi.org/10.1016/j.dendro.2014.02.002.

Sheppard, P. R., and G. C. Jacoby (1989), Application of tree-ring analysis to paleoseismology: Two case studies, *Geology*, 17(3), 226-229, doi:10.1130/0091-7613(1989)017<0226:aotrat>2.3.co;2.

Sheppard, P. R., and L. O. White (1995), Tree-ring responses to the 1978 earthquake at Stephens Pass, northeastern California, *Geology*, 23(2), 109-112, doi:10.1130/0091-7613(1995)023<0109:trrtte>2.3.co;2.

Sibson, R. H., and J. V. Rowland (2003), Stress, fluid pressure and structural permeability in seismogenic crust, North Island, New Zealand, *Geophys. J. Intern.*, 154(2), 584-594, doi:10.1046/j.1365-246X.2003.01965.x.

Sidle, R. C., and H. Ochiai (2006), Landslides. Processes, Prediction, and Land Use.

Skene, D. S. (1969), The Period of Time Taken by Cambial Derivatives to Grow and Differentiate into Tracheids in Pinus radiata: D. Don, *Ann. Bot.*, 33(2), 253-262, doi:10.1093/oxfordjournals.aob.a084280.

Smith, J. H. G. (1964), Root spread can be estimated from crown width of Doughlas Fir, Lodgepole Pine, and other British Columbia tree species, *For. Chron.*, 40(4), 456-473, doi:10.5558/tfc40456-4.

Spiecker, H. (2003), Silvicultural management in maintaining biodiversity and resistance of forests in Europe—temperate zone, *J. Environ. Man.*, 67(1), 55-65, doi:https://doi.org/10.1016/S0301-4797(02)00188-3.

Tolorza, V., Mohr, C. H., Carretier, S., Serey, A., Sepúlveda, S. A., Tapia, J., and L. Pinto (2019), Suspended sediments in Chilean rivers reveal low postseismic erosion after the Maule earthquake (Mw 8.8) during a severe drought. *J. Geophys. Res. Earth Surf.*, 124, 1378– 1397. https://doi.org/10.1029/2018JF004766 .

Tominaga, J., H. Shimada, and Y. Kawamitsu (2018), Direct measurement of intercellular CO_2 concentration in a gas-exchange system resolves overestimation using the standard method, *J. Exper. Bot.*, 69(8), 1981-1991, doi:10.1093/jxb/ery044.

Tsunogai, U., and H. Wakita (1996), Anomalous Changes in Groundwater Chemistry

Possible Precursors of the 1995 Hyogo-ken Nanbu Earthquake, Japan, J. Phys. Earth, 44(4), 381-390, doi:10.4294/jpe1952.44.381.

U.S. Geological Survey (2021), ShakeMap, M 6.9 – The Borah Peak Earthquake, accessed March 8, 2021 at URL https://earthquake.usgs.gov/earthquakes/eventpage/usp0001zbv/shakemap/pgv.

Veblen, T. T., T. Kitzberger, and A. Lara (1992), Disturbance and forest dynamics along a transect from Andean rain forest to Patagonian shrubland, J. Veg. Sci., 3(4), 507-520, doi:10.2307/3235807.

Vigny, C., et al. (2011), The 2010 M(w) 8.8 Maule Megathrust Earthquake of Central Chile, Monitored by GPS, *Science*, 332(6036), 1417-1421.

Wakita, H. (1975), Water Wells As Possible Indicators of Tectonic Strain, *Science*, 189(4202), 553-555.

Wang, C.-Y., X. Liao, L.-P. Wang, C.-H. Wang, and M. Manga (2016), Large earthquakes create vertical permeability by breaching aquitards, *Water Res. Res*., doi:10.1002/2016WR018893.

Wang, C.-Y., and M. Manga (2015), New streams and springs after the 2014 Mw6.0 South Napa earthquake, *Nature Commun.*, 6, doi:10.1038/ncomms8597.

Wang, C. Y., C. H. Wang, and M. Manga (2004), Coseismic release of water from mountains: Evidence from the 1999 (M-W=7.5) Chi-Chi, Taiwan, earthquake, *Geology*, 32(9), 769-772.

Warren, C. R., J. F. McGrath, and M. A. Adams (2001), Water availability and carbon isotope discrimination in conifers, *Oecol.*, 127(4), 476-486, doi:10.1007/s004420000609.

Wieloch, T., G. Helle, I. Heinrich, M. Voigt, and P. Schyma (2011), A novel device for batch-wise isolation of α-cellulose from small-amount wholewood samples, *Dendrochronologia*, 29(2), 115-117, doi:https://doi.org/10.1016/j.dendro.2010.08.008.

Wilson, J. P., and J. C. Gallant (2000), Terrain Analysis -Principles and Applications, 479 pp., Wiley-Blackwell Publishing, Inc.

Yadav, R. R., and P. Kulieshius (1992), Dating of Earthquakes: Tree Ring Responses to the Catastrophic Earthquake of 1887 in Alma-Ata, Kazakhstan, *Geograph. J.*, 158(3), 295-299, doi:10.2307/3060298.

Ziaco, E., F. Biondi, and I. Heinrich (2016), Wood Cellular Dendroclimatology: Testing New Proxies in Great Basin Bristlecone Pine, *Front. Plant Sci.*, 7(1602), doi:10.3389/fpls.2016.01602.

AGU PUBLICATIONS

JOURNAL OF GEOPHYSICAL RESEARCH - BIOGEOSCIENCES

Supporting Information for

Trees talk tremor – Wood anatomy and δ^{13}C content reveal contrasting tree-growth responses to earthquakes

Christian H. Mohr[1], Michael Manga[2], Gerhard Helle[3], Ingo Heinrich[3], Laura Giese[4], Oliver Korup[1]

[1]Institute of Environmental Sciences and Geography, University of Potsdam, Germany

[2]Department of Earth and Planetary Science, University of California, 307 McCone Hall, Berkeley, CA 94720, USA

[3]GFZ German Research Centre for Geosciences, Telegrafenberg, 14473 Potsdam, Germany

[4]German Federal Institute of Hydrology (BfG), 56002 Koblenz, Germany

Contents of this file

Text S1 to S2
Figures S1 to S11
Tables S1 to S7

Additional Supporting Information (Files uploaded separately)

Name	Tree ID	Growing Season	Parameter
NacPi6_2007_iso	NacPi6	2006-2007	$\delta^{13}C_{OM}$
NacPi6_2008_iso	NacPi6	2007-2008	$\delta^{13}C_{OM}$
NacPi6_2009_iso	NacPi6	2008-2009	$\delta^{13}C_{OM}$
NacPi6_2010_iso	NacPi6	2009-2010	$\delta^{13}C_{OM}$
NacPi6_2011_iso	NacPi6	2010-2011	$\delta^{13}C_{OM}$
NacPi6_2012_iso	NacPi6	2011-2012	$\delta^{13}C_{OM}$

NacPi7_2008_iso	NacPi7	2007-2008	$\delta^{13}C_{OM}$
NacPi7_2009_iso	NacPi7	2008-2009	$\delta^{13}C_{OM}$
NacPi7_2010_iso	NacPi7	2009-2010	$\delta^{13}C_{OM}$
NacPi7_2011_iso	NacPi7	2010-2011	$\delta^{13}C_{OM}$
NacPi7_2012_iso	NacPi7	2011-2012	$\delta^{13}C_{OM}$
NacPi11_2008_iso	NacPi11	2007-2008	$\delta^{13}C_{OM}$
NacPi11_2009_iso	NacPi11	2008-2009	$\delta^{13}C_{OM}$
NacPi11_2010_iso	NacPi11	2009-2010	$\delta^{13}C_{OM}$
NacPi11_2011_iso	NacPi11	2010-2011	$\delta^{13}C_{OM}$
NacPi11_2012_iso	NacPi11	2011-2012	$\delta^{13}C_{OM}$
NacPi11_2013_iso	NacPi11	2012-2013	$\delta^{13}C_{OM}$
NacPi20_2007_iso	NacPi20	2006-2007	$\delta^{13}C_{OM}$
NacPi20_2008_iso	NacPi20	2007-2008	$\delta^{13}C_{OM}$
NacPi20_2009_iso	NacPi20	2008-2009	$\delta^{13}C_{OM}$
NacPi20_2010_iso	NacPi20	2009-2010	$\delta^{13}C_{OM}$
NacPi20_2011_iso	NacPi20	2010-2011	$\delta^{13}C_{OM}$
NacPi20_2012_iso	NacPi20	2011-2012	$\delta^{13}C_{OM}$
NacPi25_2010_iso	NacPi25	2009-2010	$\delta^{13}C_{OM}$
NacPi25_2011_iso	NacPi25	2010-2011	$\delta^{13}C_{OM}$
NacPi25_2012_iso	NacPi25	2011-2012	$\delta^{13}C_{OM}$
NacPi25_2013_iso	NacPi25	2012-2013	$\delta^{13}C_{OM}$
NacPi30_2008_iso	NacPi30	2007-2008	$\delta^{13}C_{OM}$
NacPi30_2009_iso	NacPi30	2008-2009	$\delta^{13}C_{OM}$
NacPi30_2010_iso	NacPi30	2009-2010	$\delta^{13}C_{OM}$
NacPi30_2011_iso	NacPi30	2010-2011	$\delta^{13}C_{OM}$
NacPi30_2012_iso	NacPi30	2011-2012	$\delta^{13}C_{OM}$
NacPi30_2013_iso	NacPi30	2012-2013	$\delta^{13}C_{OM}$
d13C_NacPi_annual	NacPi6, NacPi7, NacPi11, NacPi20, NacPi25, NacPi30	1987/88-2012/2013	$\delta^{13}C_{OM}$
nacpi6c_2008	NacPi6	2007-2008	Lumen area
nacpi6c_2009	NacPi6	2008-2009	Lumen area
nacpi6c_2010	NacPi6	2009-2010	Lumen area
nacpi6c_2011	NacPi6	2010-2011	Lumen area

nacpi6c_2012	NacPi6	2011-2012	Lumen area
nacpi6c_2013	NacPi6	2012-2013	Lumen area
nacpi7c_2008	NacPi7	2007-2008	Lumen area
nacpi7c_2009	NacPi7	2008-2009	Lumen area
nacpi7c_2010	NacPi7	2009-2010	Lumen area
nacpi7c_2011	NacPi7	2010-2011	Lumen area
nacpi7c_2012	NacPi7	2011-2012	Lumen area
nacpi7c_2013	NacPi7	2012-2013	Lumen area
nacpi11c_2008	NacPi11	2007-2008	Lumen area
nacpi11c_2009	NacPi11	2008-2009	Lumen area
nacpi11c_2010	NacPi11	2009-2010	Lumen area
nacpi11c_2011	NacPi11	2010-2011	Lumen area
nacpi11c_2012	NacPi11	2011-2012	Lumen area
nacpi11c_2013	NacPi11	2012-2013	Lumen area
nacpi20c_2008	NacPi20	2007-2008	Lumen area
nacpi20c_2009	NacPi20	2008-2009	Lumen area
nacpi20c_2010	NacPi20	2009-2010	Lumen area
nacpi20c_2011	NacPi20	2010-2011	Lumen area
nacpi20c_2012	NacPi20	2011-2012	Lumen area

nacpi20c_2013	NacPi20	2012-2013	Lumen area
nacpi25c_2007	NacPi25	2006-2007	Lumen area
nacpi25c_2008	NacPi25	2007-2008	Lumen area
nacpi25c_2009	NacPi25	2008-2009	Lumen area
nacpi25c_2010	NacPi25	2009-2010	Lumen area
nacpi25c_2011	NacPi25	2010-2011	Lumen area
nacpi25c_2012	NacPi25	2011-2012	Lumen area
nacpi25c_2013	NacPi25	2012-2013	Lumen area
nacpi30c_2008	NacPi30	2007-2008	Lumen area
nacpi30c_2009	NacPi30	2008-2009	Lumen area
nacpi30c_2010	NacPi30	2009-2010	Lumen area
nacpi30c_2011	NacPi30	2010-2011	Lumen area
nacpi30c_2012	NacPi30	2011-2012	Lumen area
nacpi30c_2013	NacPi30	2012-2013	Lumen area

DATA. The filename is composed of the name given in the table and the ending".txt". Upper case is used for the $\boldsymbol{\delta^{13}C_{OM}}$ data (grey), while lower case is used for wood anatomic data. We are going to upload the data to a public repository, pending the final decision on this manuscript.

Introduction

Our supporting material comprises a two text sections explaining in more detail the calculation of the topographical indices we considered (S1), and presenting an overview of our $\delta^{13}C_{OM}$ sample preparation in the lab. We provide additional figures showing intra-annual time series of wood anatomy (Figures S1.3-1.6) and $\delta^{13}\mathrm{C}_{OM}$ (Figure S1.9). Further we provide a figure of residual lumen area signals the period for period 2008-2013 (Figure S1.1), the concentration of atmospheric CO_2 measured which the detrended

atmospheric CO_2 and modeled cellular CO_2 concentration build on (Figure S1.2). One additional figure depicts the modeled growing rates of *Pinus radiata* (Figure S.1.7), another one illustrates the inter-annual $\delta^{13}\mathrm{C}_{OM}$ cellulose measurements of the cored trees (Figure S.1.8). Figure S1.10 provides an additional figure of the Southern Oscillation Index (SOI) and the cross-correlation with model residuals, while Figure S1.11 presents cumulative density functions of model residuals to allow for better context (also see Table S8 for values). The supporting information also comprises a table (Table S1) with field measurements of DBH and tree height growth from Nacimiento *Pinus radiata* plantation forests (data provided by Mininco), a table providing information on tree-specific numbers of $\delta^{13}\mathrm{C}_{OM}$ samples. Table S3 provides model performance and relative variable importance of our Boosted Regression Tree approach. Table S4 and S5 present additional meteorological data and potential incoming solar radiation, respectively. Lastly, Tables S6 and S7 provide an overview of tree- and growing-season-specific wood anatomic proxies, and annually resolved $\delta^{13}C_{OM}$ values.
We also upload our intra-annually resolved $\delta^{13}C_{OM}$ and lumen area data to a public repository, pending the final decision on this manuscript.

Text S1. Topographic variables

We quantified topographic variables that explicitly account for subsurface hydrology: (1) topographic wetness index (TWI), (2) aspect, (3) distance from closest stream, (4) relative hillslope height, and (5) topographic position index (TPI). To this end we first resampled a 1-m airborne LiDAR DEM to 5-m horizontal resolution to reduce extreme values of the TWI and TPI estimates [*Jucker et al.*, 2018]. We averaged all site variables within a radius of 10 m around each tree to include the area of influence for root water uptake. Given an average tree crown diameter of <10 m [*Huber et al.*, 2010], this buffer value is motivated by observations that relate horizontal root spread and tree crown diameter [*Smith*, 1964]. Relative hillslope height refers to how near a sampled tree is to either valley bottom (0) or the ridge line (1) [*Conrad et al.*, 2015]. The TWI describes the tendency to accumulate subsurface water, though neglecting soil properties and capillarity effects [*Boehner et al.*, 2002; *Boehner and Selige*, 2006]:

$$\mathrm{TWI} = \ln\left(\frac{a}{\tan\beta}\right) \tag{1}$$

where a is upslope accumulated area and β is local slope *[Beven and Kirkby*, 1979]. The TPI measures relative topographic position as the difference between the elevation at a central point Z_0 and the mean elevation $\bar{Z}$ in a given neighborhood defined by a radius (R):

$$\mathrm{TPI} = Z_0 - \bar{Z} = Z_0 - \frac{1}{n_R}\sum_{i\in R} Z_i \tag{2}$$

where Z_i is the elevation of the DEM grid and n is the total number of surrounding pixels (n = 20) [Wilson and Gallant, 2000].

Text S2. $\delta^{13}C_{OM}$ sample preparation

We manually separated tree rings using a scalpel under a microscope. We extracted wood α-cellulose to avoid isotope variations caused by varying contents of other structural and non-structural wood fractions. We used sodium hydroxide, sodium chlorite and acetic acid to remove the extractives [*Loader et al.*, 1997] according to standard methodologies [*Schollaen et al.*, 2015; *Wieloch et al.*, 2011]. Then, we homogenized α-cellulose with an ultrasonic device and freeze-dried according to Schollaen et al. [2017], before we packed between 180 and 220 µg of cellulose into tin capsules.

First, cross-sections from the wood cores were cut with a core microtome. Second, the cross-sections (approx. 500 µm thick) were fixed in special metal frame slides and mounted on the object holder of the microdissection microscope. We used 40-80 µg of independent standards: Fluka-cellulose (100-150 µg), graphite V USGS24 and IAEA CH-7.

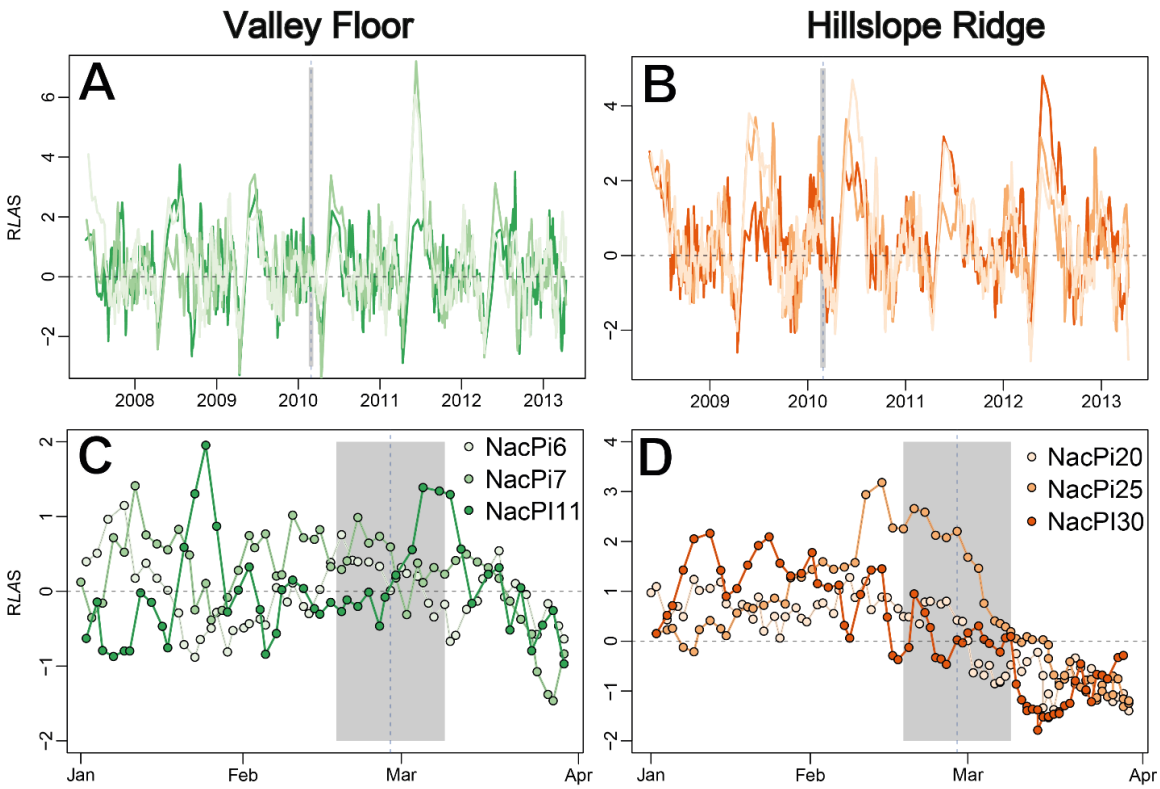

Supplementary Figure 1. Standardized *RLAS*, i.e. residual lumen area signals, for the period 2008-2013 (**a, b**) and January to April 2010 (**c, d**). Residuals refer to sinusoidal models fitted to each tree per each growing season (Figure 6 **c, d**). Green and red colors indicate single trees on the valley floor (A, B) and the ridge, respectively. Mean lumen area per tree was calculated over all eight tracheid paths. The grey bars and dashed lines show the time of the earthquake and a time window of ±10 days, respectively.

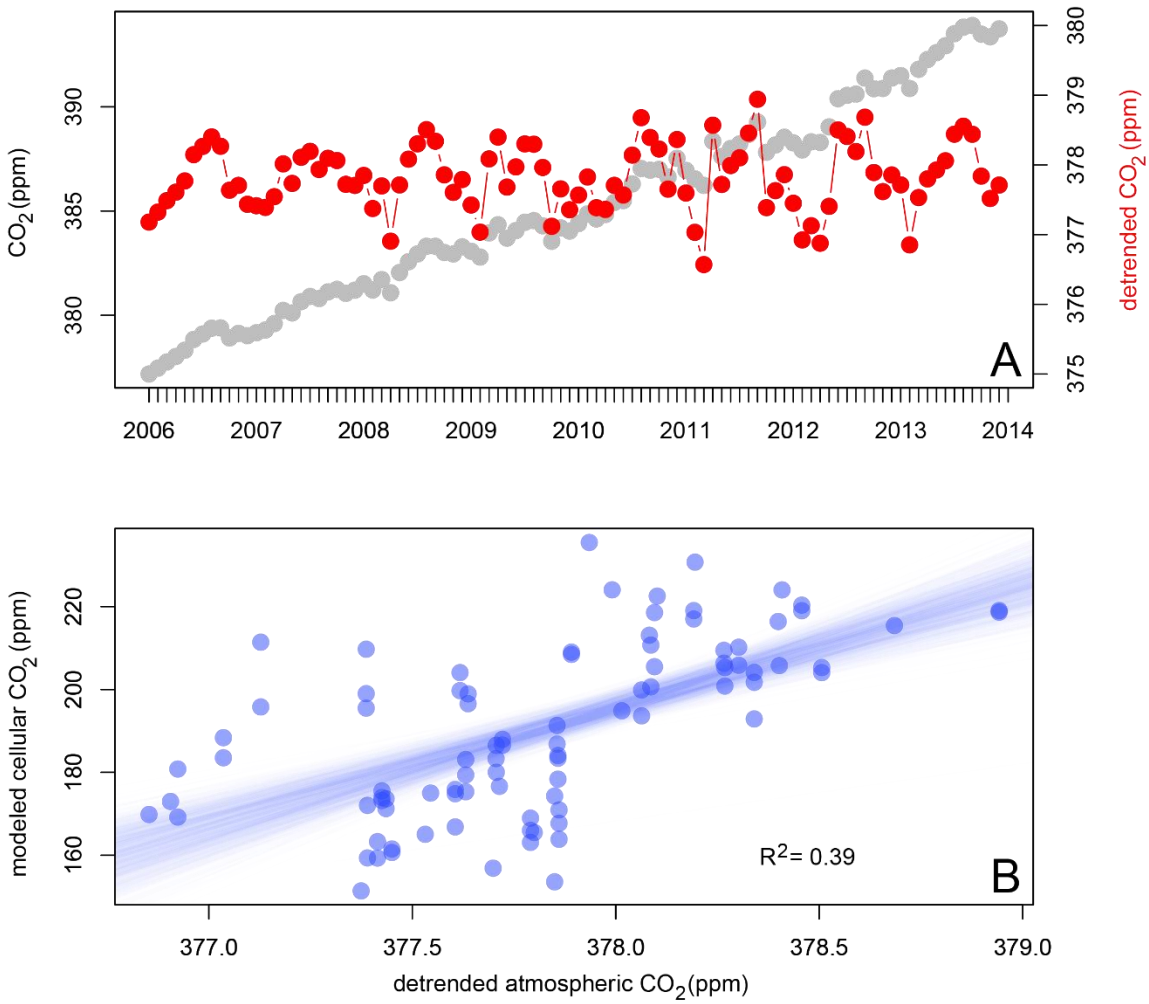

Supplementary Figure 2. A: Concentration of atmospheric CO_2 (grey dots) at Baring Head, New Zealand [*Keeling et al.*, 2001]. The red dots show detrended CO_2 concentration. B: Blue dots are measured detrended atmospheric CO_2 and modeled cellular CO_2 concentration for sample NacPi6 in 2008, 2009, 2011, and 2012. The light blue lines are n = 10,000 bootstrapped median regression models with goodness of model fit given by R^2.

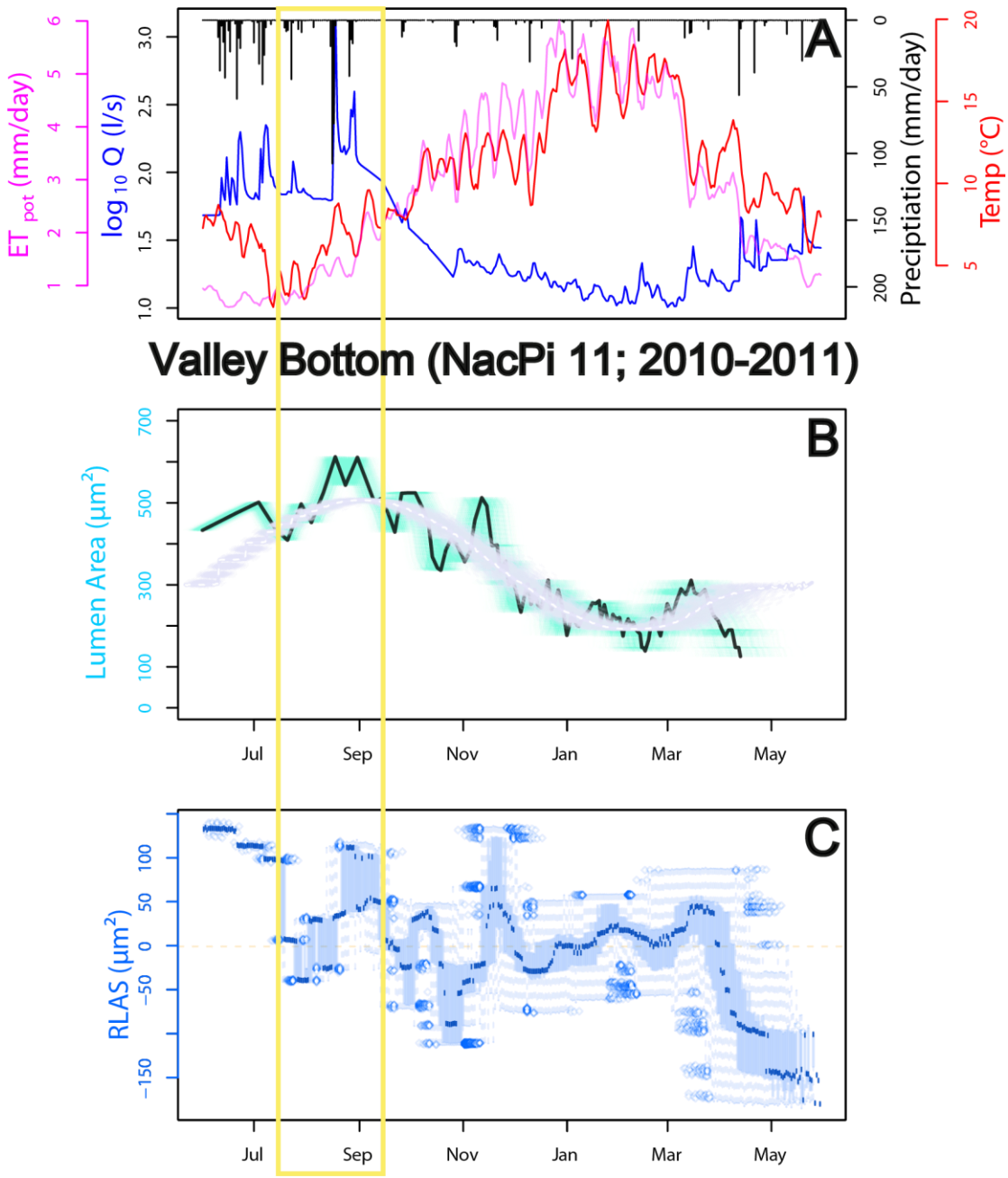

Supplementary Figure 3. a) Wood anatomy of NacPi11 for the 2010-11 growing season; streamflow discharge (in logarithmic scale) in blue, rainfall (black), and air temperature (red) for 06/2010-06/2011 measured in Pichún; Potential evapotranspiration (red lines) in Nicodahue catchment (#8362001) from the CAMEL-CL dataset [*Alvarez-Garreton et al.*, 2018]. **b)** The thick black curves are the medians of n = 10,000 MC-modeled time series of lumen area (green array of curves) and the white dashed lines are the medians of *n*=10,000 MC sine models from 06/2010 to 05/2011. **c)** The light blue boxplots are the *RLAS* binned to daily values, with the medians in dark blue. The orange bars and dashed lines mark the earthquake date ±10 days. The yellow box highlights a period where lumen area follows the rainfall and streamflow discharge patterns relatively closely (But see also Fig. S12).

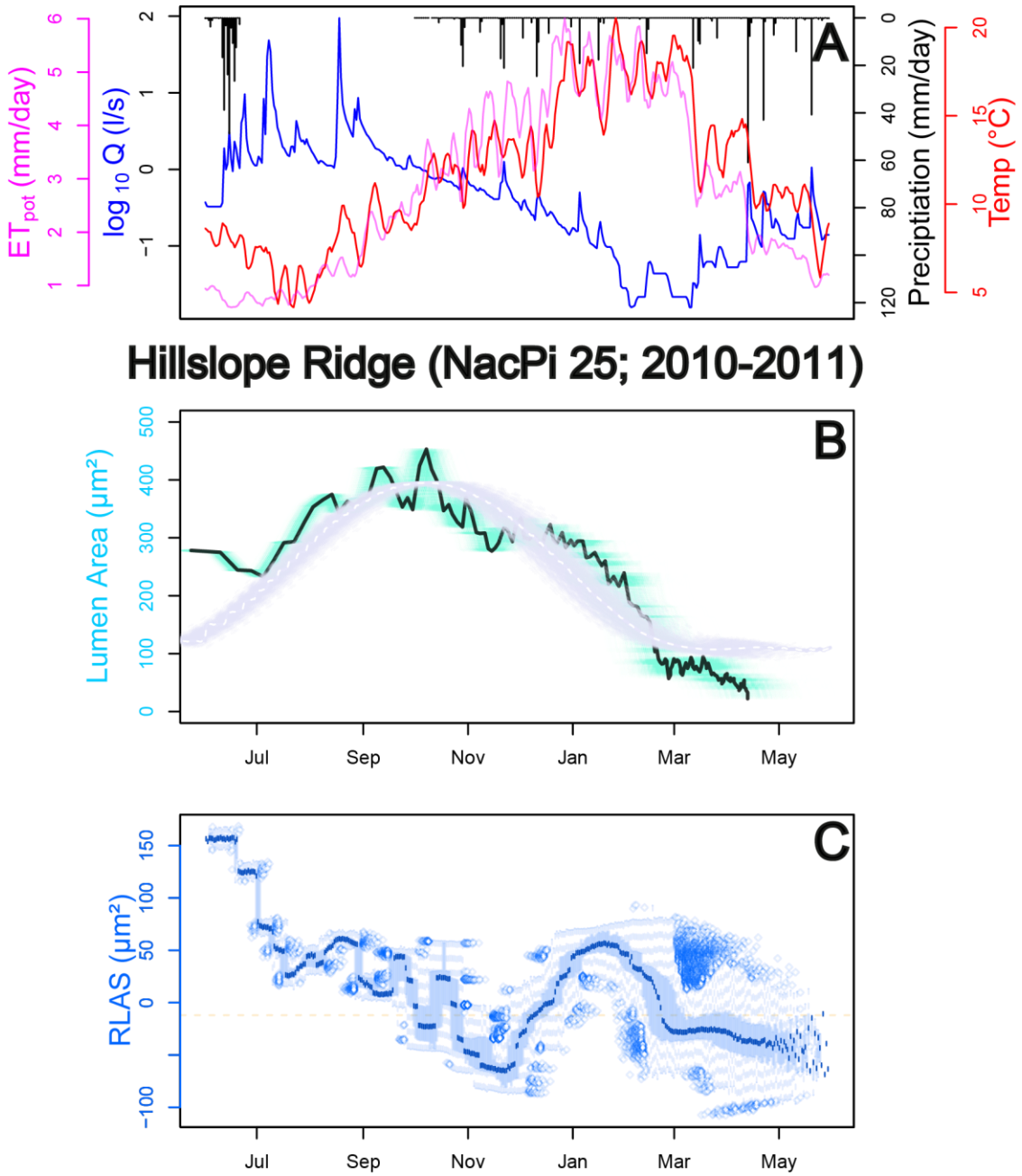

Supplementary Figure 4. Wood anatomy of NacPi25 for the 2010-11 growing season; See Supplementary Figure 3 for caption.

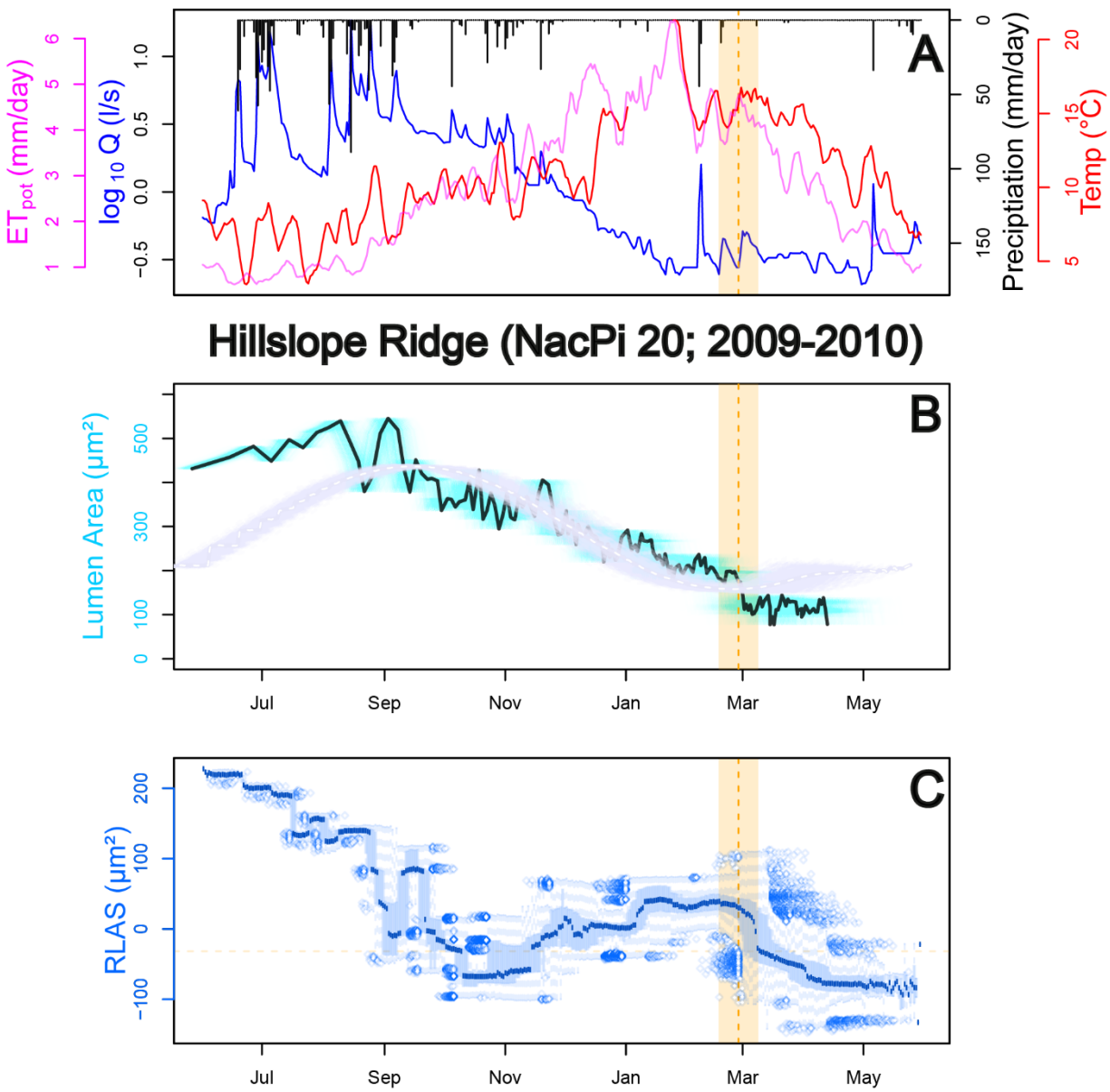

Supplementary Figure 5. Wood anatomy of NacPi20 for the 2009-10 growing season; See Supplementary Figure 3 for caption.

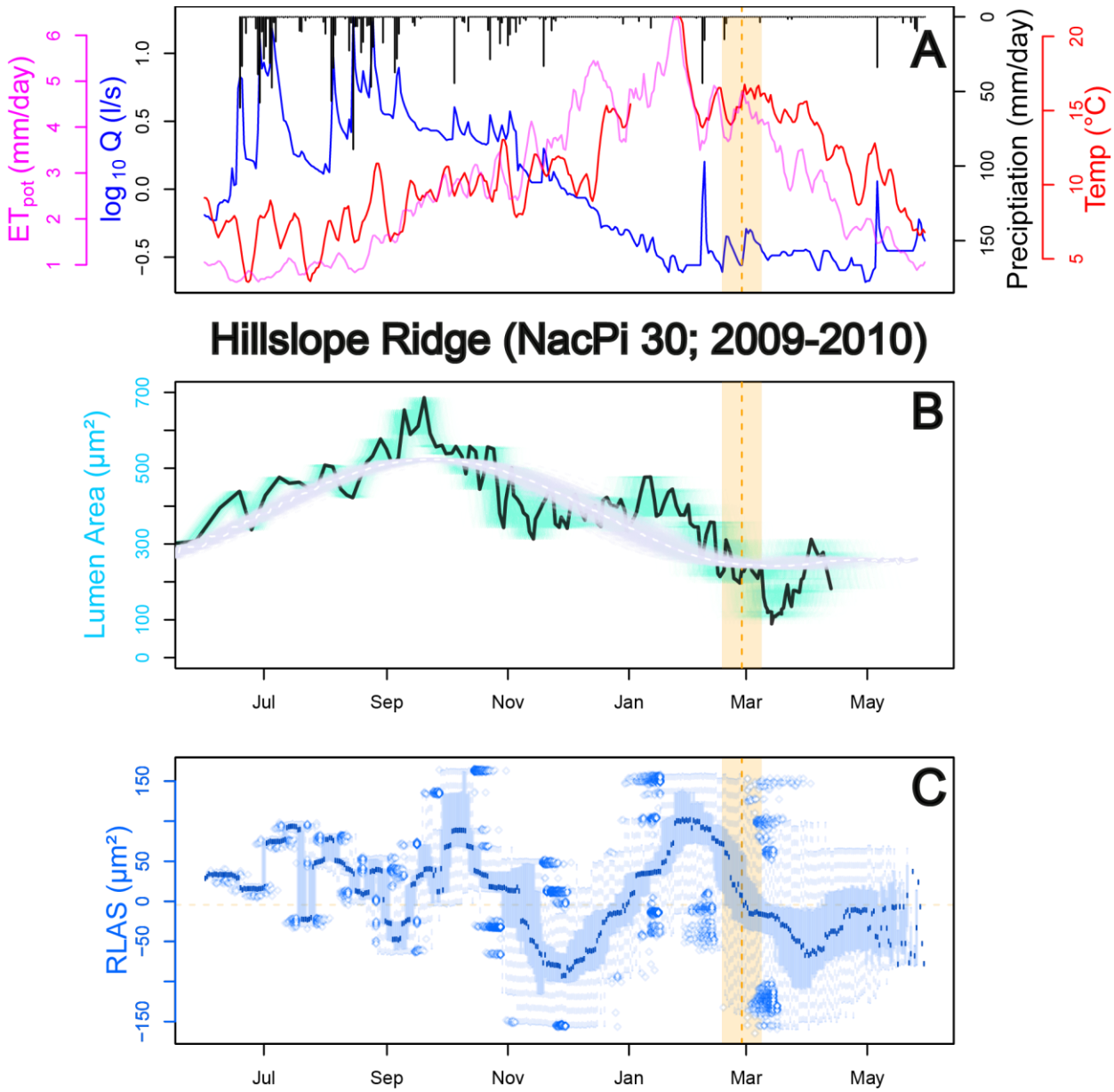

Supplementary Figure 6. Wood anatomy of NacPi30 for the 2009-10 growing season; See Supplementary Figure 3 for caption.

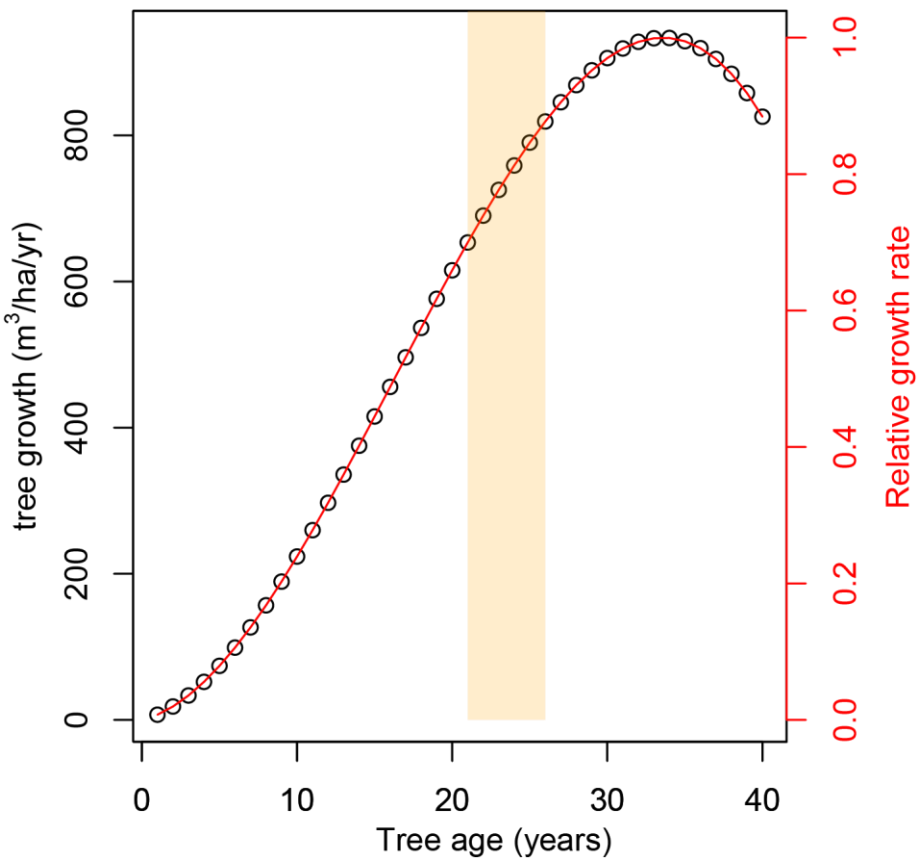

Supplementary Figure 7. Modeled absolute (m^3/ha/yr) and relative growing rates of *Pinus radiata* D.Don [*Cerda Vargas and Nuñez Sandoval*, 1996]. The orange bar indicates the time period covered by the intra-annual $\boldsymbol{\delta^{13}C_{OM}}$ samples.

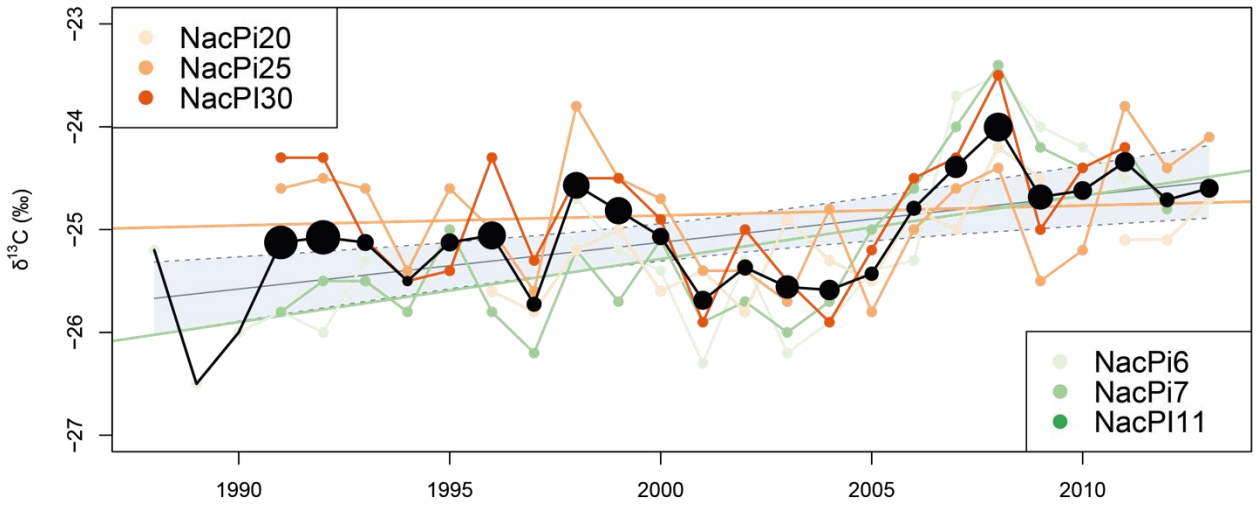

Supplementary Figure 8. Inter-annual $\boldsymbol{\delta^{13}C_{OM}}$ cellulose measurements of the cored trees separated into upper (orange) and lower slope (green) locations (y = 0.045x – 25.71, R^2 = 0.39, p-value: 0.0008). The black lines correspond to the average with the dot size scaled with the standard deviation. Note: The first three entries are only provided by NacPi6 and thus follow the black line. Grey area represents the confidence bounds (95%) with the centered median model fit.

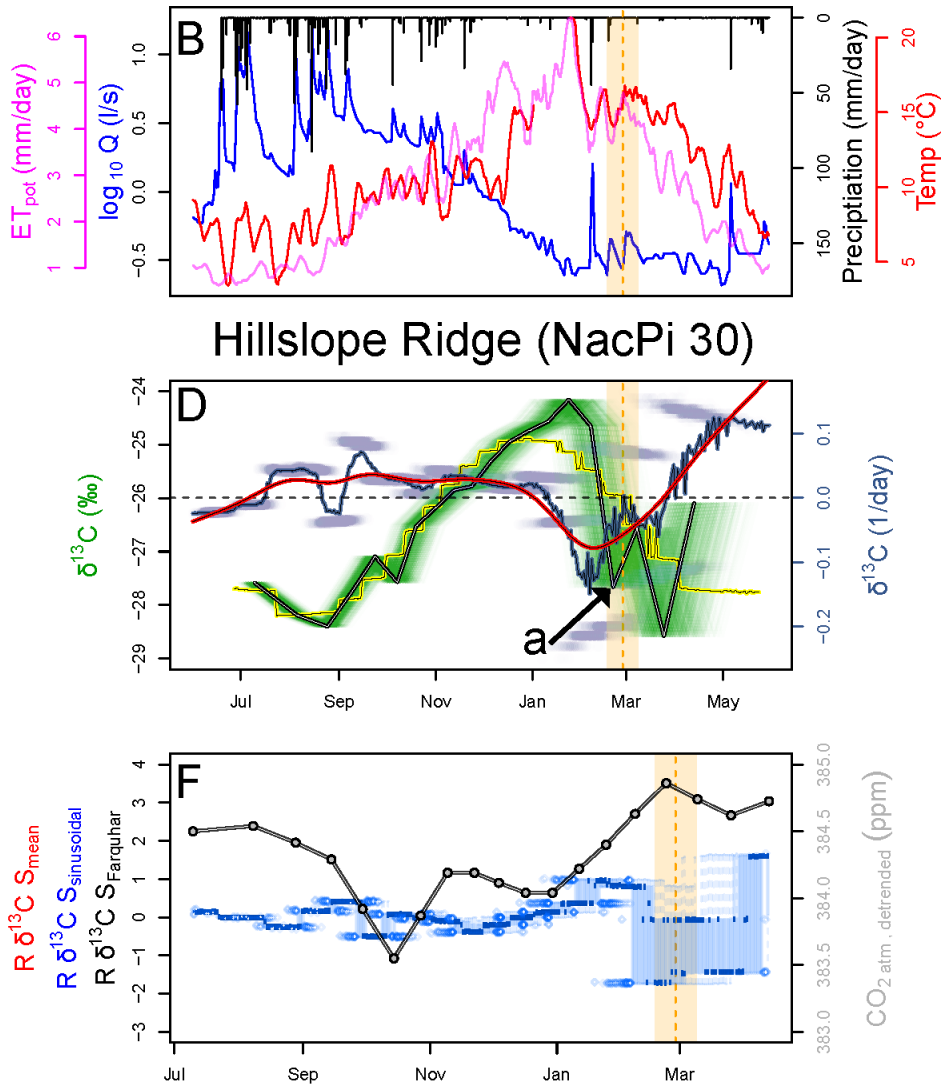

Supplementary Figure 9. Intra-annual $\boldsymbol{\delta^{13}C_{OM}}$ fractionation of NacPi30 during the growing season 2009-2010. **b)**: Time series of discharge (on logarithmic scale) in blue, rainfall (black), air temperature (red), and potential evapotranspiration (pink). Data on streamflow discharge, rainfall, and air temperature from S.A. ; potential evapotranspiration from Nicodahue catchment (#8362001) of CAMEL-CL data [*Alvarez-Garreton et al.*, 2018]. The orange bars and dashed lines mark the earthquake date ±10 days. **d)** The black curve is the median of all MC-modeled time series of $\boldsymbol{\delta^{13}C_{OM}}$ (n = 10,000, green array of curves) of NacPi30. Daily rates of $\boldsymbol{\delta^{13}C_{OM}}$ change are violet points with violet solid line showing medians and red dashed line showing spline regression. The yellow curves are medians of *n*=10,000 MC- sinusoidal–models per sampled cellulose increments. **f)** Residual $\boldsymbol{\delta^{13}C_{OM}}$ signals (R$\boldsymbol{\delta^{13}C_{OM}}$S); grey and red bars are $\boldsymbol{\delta^{13}C_{OM}}$-residuals to of the Farquhar-models and residuals between observed $\boldsymbol{\delta^{13}C_{OM}}$-values and the annual mean, respectively. The blue boxplot time series are daily $\boldsymbol{\delta^{13}C_{OM}}$-residuals of sinusoidal model. The grey dotted curves are de-trended atmospheric CO_2 (ppm) measured at Baring Head, New Zealand [*Keeling et al.*, 2001].

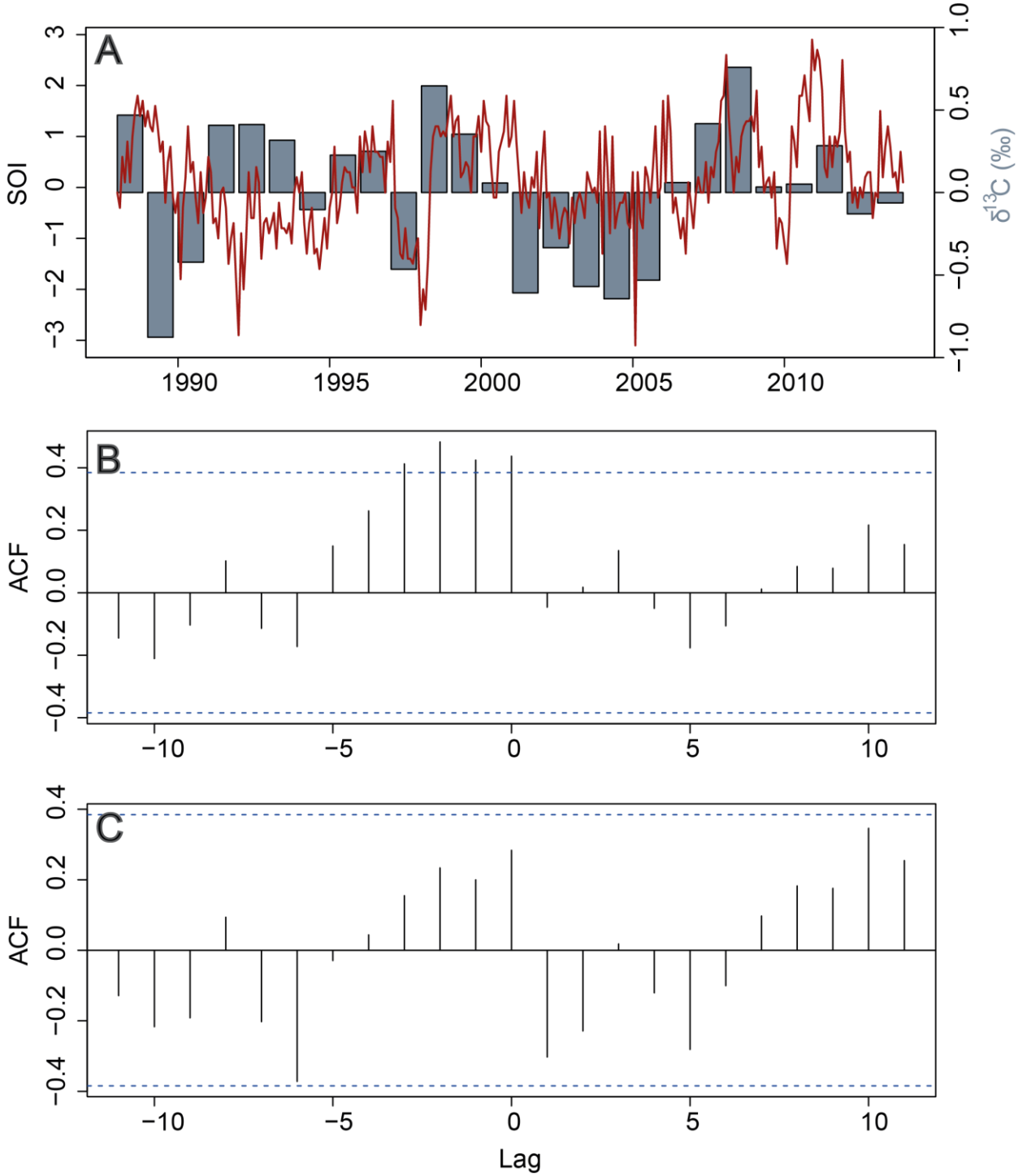

Supplementary Figure 10. Time series of $\boldsymbol{\delta^{13}C_{OM}}$-model residuals and Southern Oscillation Index (SOI). **a)** Grey bars correspond to the model residuals to account for detrended atmospheric CO_2 concentrations (see Supplementary Figure 2), the red line depicts the monthly Southern Oscillation Index SOI (downloaded from https://www.ncdc.Noaa.gov /teleconnections/enso/indicators/soi, 02/14/2020). **b)** Cross correlation between annually resolved $\boldsymbol{\delta^{13}C_{OM}}$ values and SOI; C: cross correlation between model

residuals of linear trend (Supplementary Figure 2) and SOI. We used the R package rsoi (https://cran.r-project.org/web/packages/rsoi/rsoi.pdf)

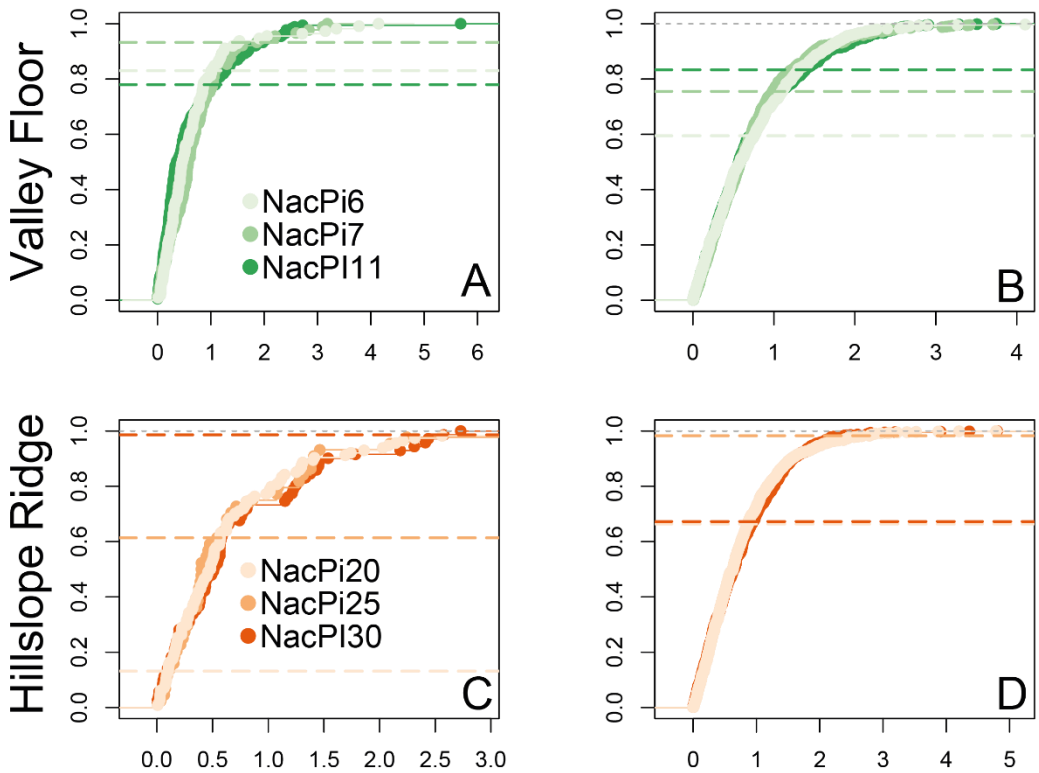

Supplementary Figure 11. Empirical cumulative density functions of absolute, standardized model residuals for $\boldsymbol{\delta^{13}C_{OM}}$ (**a, c**) and lumen area (**b, d**) for the valley bottom and hillslope ridge. All data are standardized to the specific tree. Green colors refer to valley floor, reddish color to ridge. Marked horizontal lines show the empirical frequencies for the residuals assigned to the first sample-date of the earthquake for $\boldsymbol{\delta^{13}C_{OM}}$. See Supplementary Table 8 for values.

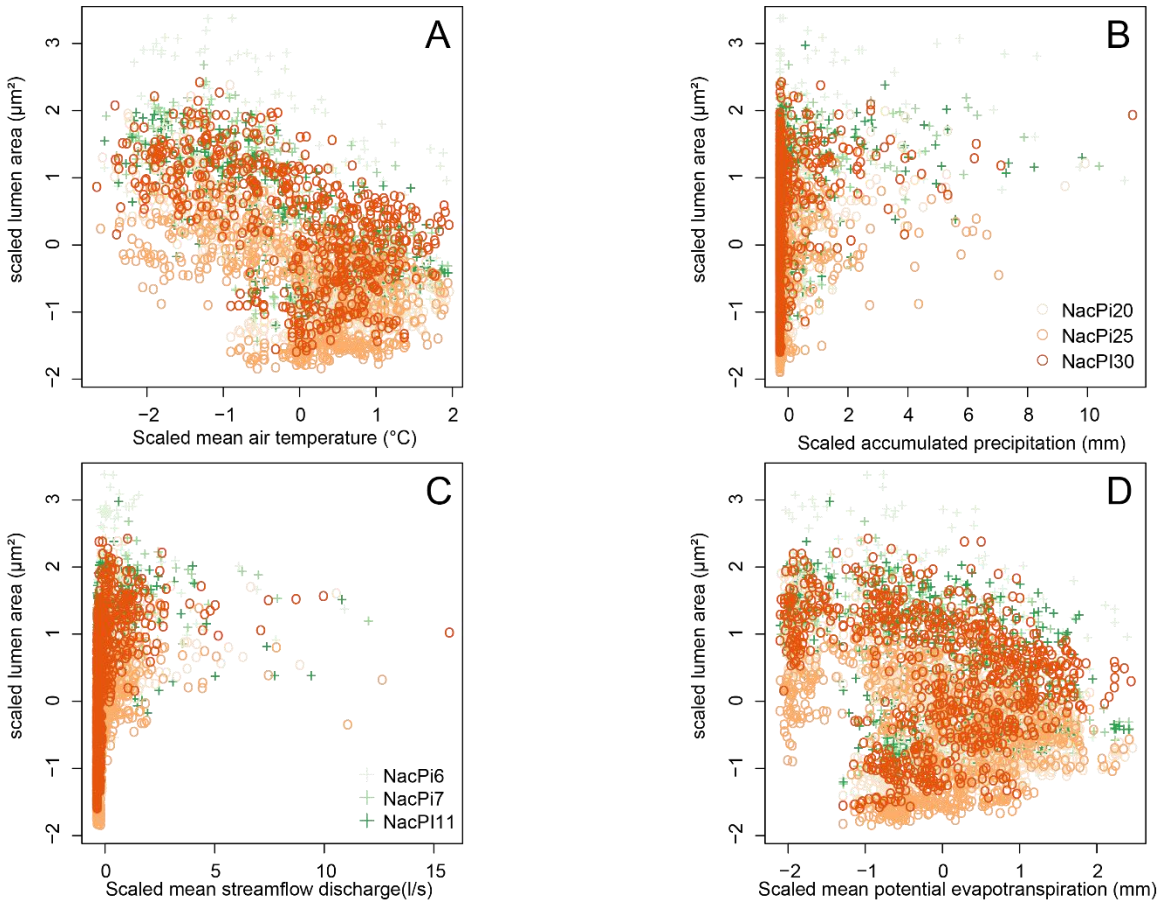

Supplementary Figure 12. Scaled lumen area (µm^2) as a function of (A) mean air temperature (°C), (B) accumulated precipitation (mm), (C) mean streamflow discharge (l/s), and (D) mean potential evapotranspiration (mm). Air temperature, precipitation, streamflow and potential evapotranspiration are estimated for the time periods needed for cell formation.

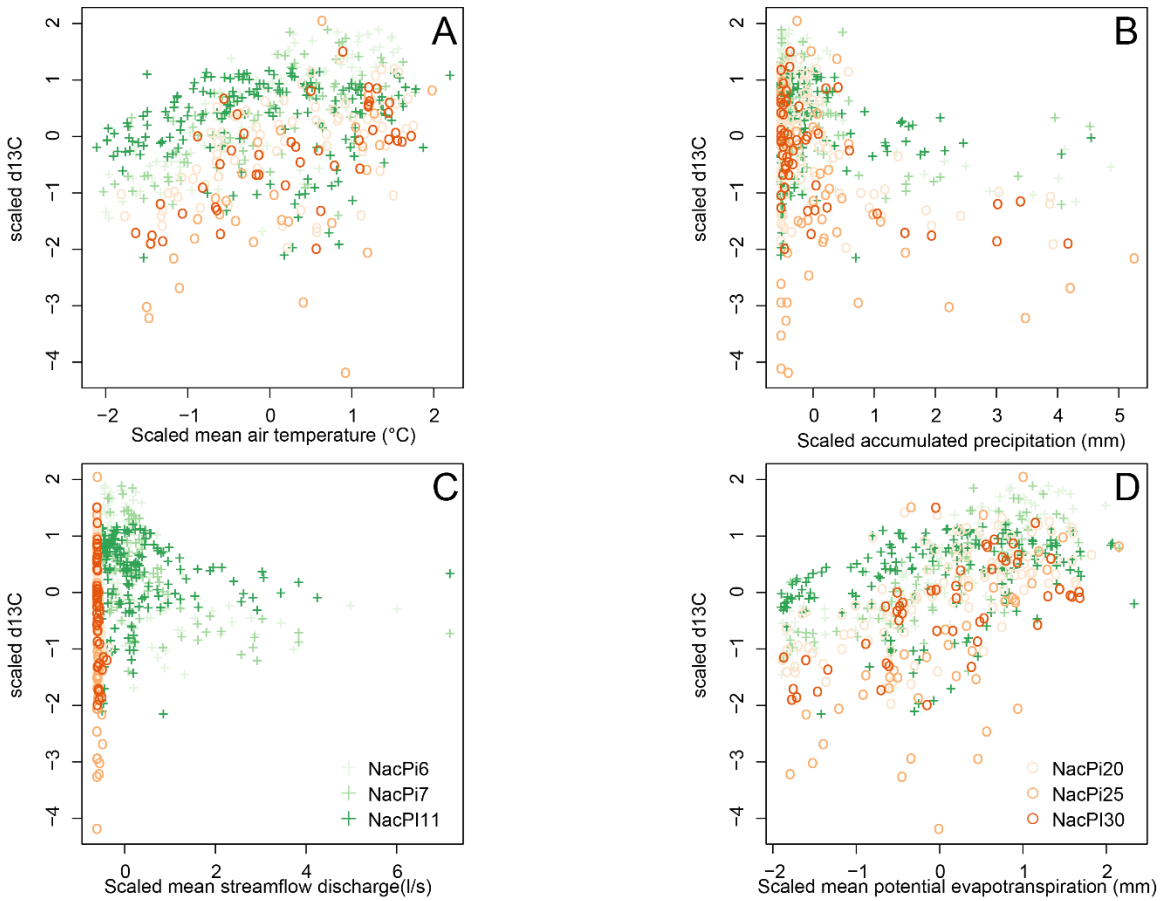

Supplementary Figure 13. Scaled $\delta^{13}C_{OM}$ as a function of (A) mean air temperature (°C), (B) accumulated precipitation (mm), (C) mean streamflow discharge (l/s), and (D) mean potential evapotranspiration (mm). Air temperature, precipitation, streamflow and potential evapotranspiration are estimated for the time periods needed for cell formation.

Month	Cumulative DBH growth (cm)	Cumulative height growth (cm)
Jun	2.5	3.8
Jul	5.8	7.8
Aug	11.8	13.8
Sep	22.3	25.8
Oct	34.3	41.3
Nov	44.3	59
Dec	56.3	74
Jan	67.3	82
Feb	78.1	88
March	89.1	92.1
Apr	95.1	95.9
May	98.6	99.9

Supplementary Table 1. Field measurements of DBH and tree height growth from Nacimiento Pinus radiata plantation forests, data provided by Mininco.

Year	NacPi6	NacPi7	NacPi11	NacPi20	NacPi25	NacPi30
2006/07	17	-	-	26	-	-
2007/08	14	31	42	17	-	22
200809	25	32	32	28	-	23
2009/10	25	34	35	28	11	20
2010/11	27	17	35	19	10	13
2011/12	21	21	51	14	16	15
2012/13	14	-	28	-	9	17
Σ	143	135	223	132	46	110

Supplementary Table 2. Number of $\boldsymbol{\delta^{13}C_{OM}}$ samples for each tree and growing season

Site	$ridge_{pre}$	$ridge_{post}$	$valley_{pre}$	$valley_{post}$
R^2	0.78	0.46	0.63	0.83
Individual Tree	11.9	3.5	12.9	6.0
Accum. Precipitation	4.8	16.3	9.0	24.9
Max. Precipitation	5.3	7.8	3.4	8.9
Mean Precipitation	4.6	9.4	2.7	7.5
Solar Radiation	32.1	24.8	40.7	29.7
Mean Air Temperature	23.0	16.2	8.6	6.3
Mean Discharge	18.3	21.9	22.7	16.7

Supplementary Table 3. Model performance (R^2) and relative variable importance of the $\delta^{13}C_{OM}$-Boosted Regression Tree models. Note: Mean discharge recorded at the catchment outlets during said period. Note: Solar radiation here as "Potential Incoming Solar Radiation" and derived from topography [*Conrad et al.,* 2015], see also Supplementary Table 5.

Growing season	Mean °C	Accumulated rainfall (mm)
2008-9	10.95±3.39	756
2009-10	10.37±3.25	1177
2010-11	10.77±3.36	888
2011-12	11.51±3.84	1062
2012-2013	11.51±3.72	670

Supplementary Table 4. Mean annual air temperatures (°C) and accumulated rainfall registered at the nearest meteorological stations at Pichún. The long term mean annual air temperature is 11.0 ± 3.8 °C (01/1979-12/2016) (CAMEL-CL, *Alvarez-Garreton et al.* [2018]).

Tree ID	Potential solar radiation (kWh/m^2 yr^{-1})
NacPi6	1975.5±111.3
NacPi7	19.94.6±120.4
NacPi11	2137.6±32.3
NacPi20	2007.0±12.5
NacPi25	2079.5±11.0
NacPi30	2055.9±15.5

Supplementary Table 5. Modeled annual potential incoming solar radiation [*Böhner and Antonić*, 2009; *Conrad et al.*, 2015], i.e. the all-year sum of direct and diffuse insolation, within a 10-m buffer around each cored tree during the period 01/01/2010-12/31/2010. Calculation has been performed at a 2h resolution; lumped atmospheric transmittance is assumed as 70%; local sky factor was calculated using the 5m DEM [*Conrad et al.*, 2015]. Values were calculated using the potential incoming solar radiation algorithm implemented in SAGA-GIS (http://www.saga-gis.org/saga_tool_doc/2.2.2/ta_lighting_2.html). The algorithm recognized three main governing factors: (1) relative orientation of the Earth in relation to the sun, (2) clouds and other atmospheric inhomogeneity, such as dust, and (3) topography.

Proxy	Growing season	NacPi6	NacPi7	NacPi11	NacPi20	NacPi25	NacPi30
Early wood (%)	2008-2009	48.63	53.38	51.13	59.25	45.38	67.63
	2009-2010	53.88	83.88	76.25	63.38	57.00	73.63
	2010-2011	68.38	78.50	79.38	71.25	60.38	73.38
	2011-2012	64.63	71.44	59.00	62.63	50.00	72.75
	2012-2013	62.63	59.38	60.38	82.13	47.56	77.63
Mean early wood (µm)	2008-2009	402.82	312.29	403.13	310.67	259.47	435.03
	2009-2010	424.48	392.54	383.07	284.34	323.18	449.07
	2010-2011	406.72	404.41	447.86	318.72	317.37	421.21
	2011-2012	423.13	456.61	386.23	329.04	309.04	403.69
	2012-2013	559.00	407.79	383.44	318.16	243.17	405.45
Mean tree ring width (mm)	2008-2009	2.59	5.60	5.92	2.63	1.84	3.75
	2009-2010	3.83	4.86	5.04	4.00	2.06	4.37
	2010-2011	3.89	3.65	5.87	3.79	1.73	2.76
	2011-2012	4.18	2.78	5.77	2.58	1.84	2.23
	2012-2013	3.09	2.42	8.88	2.33	1.89	2.30
Number of cells	2008-2009	110.00	215.00	210.00	125.00	90.00	130.00
	2009-2010	150.00	160.00	170.00	170.00	80.00	140.00
	2010-2011	140.00	120.00	200.00	165.00	75.00	100.00
	2011-2012	140.00	80.00	200.00	120.00	90.00	80.00
	2012-2013	110.00	80.00	300.00	100.00	80.00	80.00
Mean lumen area (μm^2)	2008-2009	254.74	242.10	311.37	236.12	156.76	353.38
	2009-2010	303.14	372.55	353.56	233.96	227.62	395.35
	2010-2011	334.44	363.37	410.83	261.01	223.46	358.38
	2011-2012	352.82	387.95	315.86	255.47	191.17	332.23
	2012-2013	415.42	315.32	316.41	288.24	171.80	350.27

Supplementary Table 6. Absolute mean (µm) and relative (%) early wood and number of cells, tree ring width (mm), and lumen area (µm2) averaged from *n*=8 paths for the sampled trees during respective growing seasons.

Year	NacPi6	NacPi7	NacPi11	NacPi20	NacPi25	NacPi30
1987/88	-25.2	NO DATA	NO DATA	NO DATA	NO DATA	NO DATA
1988/89	-26.5	NO DATA	NO DATA	NO DATA	NO DATA	NO DATA
1989/90	-26	NO DATA	NO DATA	NO DATA	NO DATA	NO DATA
1990/91	-25.8	-25.8	NO DATA	-24.6	-24.3	NO DATA
1991/92	-26	-25.5	NO DATA	-24.5	-24.3	NO DATA
1992/93	-25.3	-25.5	NO DATA	-24.6	-25.1	NO DATA
1993/94	NO DATA	-25.8	NO DATA	-25.4	-25.5	-25.3
1994/95	NO DATA	-25	NO DATA	-24.6	-25.4	-25.5
1995/96	NO DATA	-25.8	-25.6	-25	-24.3	-24.6
1996/97	NO DATA	-26.2	-25.8	-25.6	-25.3	-25.7
1997/98	-24.7	-25.2	-25.2	-23.8	-24.5	-24
1998/99	-25.2	-25.7	-25	-24.5	-24.5	-24
1999/00	-25.4	-25.1	-25.6	-24.7	-24.9	-24.7
2000/01	-26.3	-25.9	-25.4	-25.4	-25.9	-25.2
2001/02	-25.3	-25.7	-25.8	-25.4	-25	-25
2002/03	-26.2	-26	-24.9	-25.7	-25.5	-25
2003/04	-25.9	-25.7	-25.3	-24.8	-25.9	-25.9
2004/05	-25.4	-25	-25.5	-25.8	-25.2	-25.7
2005/06	-25.3	-24.6	-24.8	-25	-24.5	-24.5
2006/07	-23.7	-24	-25	-24.6	-24.3	-24.7
2007/08	-23.5	-23.4	-24.2	-24.4	-23.5	-25
2008/09	-24	-24.2	-24.5	-25.5	-25	-24.9
2009/10	-24.2	-24.4	NO DATA	-25.2	-24.4	-24.9
2010/11	-24.5	-24.2	-25.1	-23.8	-24.2	-24.3
2011/12	NO DATA	-24.8	-25.1	-24.4	NO DATA	-24.5
2012/13	NO DATA	NO DATA	-24.7	-24.1	NO DATA	-25

Supplementary Table 7. Annual $\boldsymbol{\delta^{13}C_{OM}}$ values. NO DATA refers to no measured data available for the respective growing season.